Developmental Cell
Article

The Diaphragms of Fenestrated Endothelia: Gatekeepers of Vascular Permeability and Blood Composition

Radu V. Stan,[1,2,6,7,*] Dan Tse,[1] Sophie J. Deharvengt,[1] Nicole C. Smits,[3,6] Yan Xu,[1] Marcus R. Luciano,[1] Caitlin L. McGarry,[1] Maarten Buitendijk,[8] Krishnamurthy V. Nemani,[5] Raul Elgueta,[2] Takashi Kobayashi,[3,6] Samantha L. Shipman,[3,6] Karen L. Moodie,[3,6] Charles P. Daghlian,[1] Patricia A. Ernst,[2,4,7] Hong-Kee Lee,[1] Arief A. Suriawinata,[1] Alan R. Schned,[1] Daniel S. Longnecker,[1] Steven N. Fiering,[2,4,7] Randolph J. Noelle,[2,7] Barjor Gimi,[5] Nicholas W. Shworak,[3,6] and Catherine Carrière[3,7]
[1]Department of Pathology
[2]Department of Microbiology and Immunology
[3]Department of Medicine
[4]Department of Genetics
[5]Department of Radiology
[6]Heart and Vascular Research Center
[7]Norris Cotton Cancer Center
[8]Program in Experimental and Molecular Medicine
Geisel School of Medicine at Dartmouth, Hanover, NH 03756, USA
*Correspondence: radu.v.stan@dartmouth.edu
http://dx.doi.org/10.1016/j.devcel.2012.11.003

SUMMARY

Fenestral and stomatal diaphragms are endothelial subcellular structures of unknown function that form on organelles implicated in vascular permeability: fenestrae, transendothelial channels, and caveolae. PV1 protein is required for diaphragm formation in vitro. Here, we report that deletion of the PV1-encoding *Plvap* gene in mice results in the absence of diaphragms and decreased survival. Loss of diaphragms did not affect the fenestrae and transendothelial channels formation but disrupted the barrier function of fenestrated capillaries, causing a major leak of plasma proteins. This disruption results in early death of animals due to severe noninflammatory protein-losing enteropathy. Deletion of PV1 in endothelium, but not in the hematopoietic compartment, recapitulates the phenotype of global PV1 deletion, whereas endothelial reconstitution of PV1 rescues the phenotype. Taken together, these data provide genetic evidence for the critical role of the diaphragms in fenestrated capillaries in the maintenance of blood composition.

INTRODUCTION

Microvascular permeability is a vital function by which endothelial cells (ECs) in combination with their glycocalyx and basement membranes from capillaries and postcapillary venules (the so-called exchange segment of the vascular tree), control the exchange of molecules between the blood plasma and the interstitial fluid, while maintaining blood and tissue homeostasis (Bates, 2010; Dvorak, 2010; Komarova and Malik, 2010; Levick and Michel, 2010). A clear understanding of the molecular mechanisms involved in the control of microvascular permeability continues to elude us, fueling persisting controversy as to which pathways are employed by different molecules in order to cross the endothelial barrier (Predescu et al., 2007; Rippe et al., 2002). To cross the EC monolayer proper, molecules use either a paracellular (i.e., in between the cells) or a transcellular (i.e., across the cells) route. Transcellular exchange is accomplished via either solute transporters, or transcytosis via vesicular carriers (e.g., caveolae), or pore-like subcellular structures (i.e., fenestrae and transendothelial channels [TECs]) (for review, see Aird, 2007; Tse and Stan, 2010).

A large part of the problem is the lack of understanding of the function of the different endothelial subcellular structures involved in permeability, adopted by ECs in the exchange segment of different vascular beds (Aird, 2007; Tse and Stan, 2010). Among these structures are caveolae, fenestrae, and TECs. Fenestrae are 60–80 nm diameter transcellular pores spanned by fenestral diaphragms (FDias), except in the ECs of kidney glomerulus and the liver sinusoids (Clementi and Palade, 1969a; Reeves et al., 1980; Wisse, 1970). FDias consist of radial fibrils (Bearer and Orci, 1985) and display tufts of heparan sulfate proteoglycans on their luminal side (Simionescu et al., 1981). TECs thought to be fenestrae precursors, occur interspersed with fenestrae in attenuated areas of the ECs albeit at approximately 5- to 20-fold lower surface density, depending on the vascular bed (Milici et al., 1985). TECs are spanned by two diaphragms without heparan sulfate proteoglycan tufts (Rostgaard and Qvortrup, 1997). Caveolae are plasma membrane invaginations, which in ECs of select vascular beds (i.e., lung and all fenestrated ECs) display a thin protein barrier-like structure in their necks called a stomatal diaphragm (SDia) (Stan et al., 1999a).

FDias occur at sites where molecules are adsorbed from the interstitium into the blood stream (i.e., endocrine glands, kidney

peritubular capillaries, and intestine villi). Tracer experiments (Clementi and Palade, 1969a) as well as whole organ studies (Levick and Smaje, 1987) have suggested that FDias and the "glycocalyx tufts" present on their luminal side, form a combined filter acting as a permselective barrier allowing the passage of water and small molecules (i.e., ions, sugars, amino acids, small peptide hormones) and blocking the extravasation of macromolecules (for review, see Levick and Michel, 2010). Although information exists on the molecular diameter cut-off of the basement membrane, opinions vary as to the contribution of proteoglycans and diaphragm to the filter (Bearer and Orci, 1985; Levick and Smaje, 1987). Tracer studies also hint to a barrier function for SDias in caveolae (Clementi and Palade, 1969a; Villaschi et al., 1986) but the physiological implications are still unclear. There is little knowledge on the precise function of TECs.

The removal of a long-standing obstacle in studying the function of endothelial diaphragms was initiated by proteomic studies identifying a homodimeric endothelial membrane glycoprotein, namely PV1, as the first known molecular component of both FDias and SDias (Stan, 2004; Stan et al., 1997, 1999a, 1999b). PV1 protein is encoded by the vertebrate gene plasmalemma vesicles associated protein (*Plvap*) (Stan et al., 2001; Tse and Stan, 2010). PV1 is necessary to form FDias and SDias in cells in culture (Ioannidou et al., 2006; Stan et al., 2004). Moreover, formation of FDias and SDias appears to be the sole cellular function of PV1 in ECs (Tkachenko et al., 2012). Recently, the deletion of PV1 in mice was reported confirming the role of PV1 in forming both FDias and SDias in vivo (Herrnberger et al., 2012a, 2012b). A model by which the FDias and SDias are similar structures consisting of a framework of radial fibrils made of PV1 homodimers was proposed (Tse and Stan, 2010). However, this model is not a matter of general consensus, other studies disputing the role of PV1 in diaphragm formation (Hnasko and Ben-Jonathan, 2005; Hnasko et al., 2006a).

With the exception of two reports (Hnasko et al., 2006b, 2002), most data agree on PV1 being an endothelial-specific protein (for review, see Tse and Stan, 2010). This is also supported by PV1 being the antigen of two classic "anti-endothelial" monoclonal antibodies MECA-32 (Hallmann et al., 1995) and PAL-E (Niemelä et al., 2005) and studies of LacZ knockin in *Plvap* locus in mice (Herrnberger et al., 2012a, 2012b). PV1 has emerging roles in cancer (Carson-Walter et al., 2005; Deharvengt et al., 2012; Madden et al., 2004), diapedesis of leukocytes in sites of inflammation (Keuschnigg et al., 2009), inflammatory (Mozer et al., 2010), and ocular disease (Chen et al., 2012; Paes et al., 2011; Schäfer et al., 2009).

Herein, we exploit the obligate role of PV1 in diaphragm formation to examine in vivo the role of FDias in the maintenance of permselectivity in fenestrated endothelia and thereby in blood plasma composition. Using independently generated mice with loss and gain of PV1 function, we also confirm that endothelial PV1 is required for diaphragm formation in vivo, and that the diaphragms in organs with fenestrated vessels are essential for maintaining endothelial barrier function, basal permeability and blood composition. Impairment of FDia function in PV1 deficient mice leads to selective loss of plasma proteins with consequent edema and dyslipidemia, gradually resulting in multiple organ dysfunction. PV1 deficient mice succumb to a lethal, noninflammatory, protein-losing enteropathy. Thus, PV1-mediated endothelial barrier function is critical for mammalian survival.

RESULTS

PV1 Is Essential for Intrauterine and Postnatal Survival

To determine the function of PV1 protein and endothelial diaphragms in vivo, mice were generated that carried *LoxP* sites inserted into introns 1 and 5 of the mouse *Plvap* locus ($PV1^{L/L}$ mice) (Figure 1A; Figure S1A available online). By breeding the $PV1^{L/L}$ mice with *CMV-cre* mice, which express the cre recombinase under the control of the ubiquitously activated cytomegalovirus-derived promoter (CMV), we generated $PV1^{-/-}$ mice, lacking PV1 in all tissues (Figures 1A, S1B, and S1C). PV1 absence following disruption of the *Plvap* gene was confirmed at mRNA (Figure 1B) and protein level (Figure 1C).

Homozygous disruption of the *Plvap* gene led to sharply decreased survival that varied depending on the mouse strain used. On pure C57Bl/6J background, PV1 deletion resulted in 100% lethality between embryonic day 13 (embryonic day E13) and postnatal day 2 (P2). On hybrid intercrosses containing a mix of Balb/c (50%), C57Bl/6J (37.5%), and 129Sv/J (12.5%) backgrounds, ~20% of the expected frequency of homozygous $PV1^{-/-}$ mice survived up to 3–4 months of age (Figures 1D and 1E). The heterozygote $PV1^{+/-}$ had decreased PV1 mRNA (Figure 1B) and protein levels (Figure 5B), but did not exhibit any obvious phenotype on either C57BL/6J or mixed backgrounds. All the subsequent experiments in $PV1^{-/-}$ mice were carried out on mixed Balb/c-C57Bl/6J-129Sv/J background because it was the only one that allowed the study of postnatal $PV1^{-/-}$ phenotype.

At birth, $PV1^{-/-}$ mice displayed normal appearance and normal size but gradually developed signs of growth retardation and wasting. Decreased average body weight was significant in both genders by P4 progressing in severity as the mice aged (Figure S1D). Four-week-old $PV1^{-/-}$ mice had ~30%–40% reduction in body weight (Figure S1D) and ~15% in body length (Figures S1E and S1F). The small body size was accompanied by a generalized decrease in white adipose tissue deposits in the abdominal wall, retroperitoneal, and gonadal fat pads as shown by MRI in 3- to 4-week-old live $PV1^{-/-}$ mice (Figure S1G) and a reduced gonadal fat pad/body weight ratio postmortem (Figure S1H). By that age, $PV1^{-/-}$ mice also developed a distended abdomen due to accumulation of ascites (data not shown). Aside from an abnormally bent tail observed in ~70% of mutant mice (Figure S1E), no defect in organ appearance and size (as determined by organ/body weight ratio, data not shown) were observed at birth in $PV1^{-/-}$ mice. Past 1 week of age, $PV1^{-/-}$ pancreata displayed an abnormally reduced size as evidenced by pancreas/body weight ratio (Figure S1I). All organs, including the pancreas, had normal histological appearance (Figure S2A).

PV1 Is Essential for the Formation of Endothelial Diaphragms In Situ

In vitro studies have shown that PV1 is required for diaphragm formation (Ioannidou et al., 2006; Stan et al., 2004) suggesting that PV1 loss in vivo would prevent diaphragm formation in fenestrae, TECs, and caveolae. To confirm this critical finding,

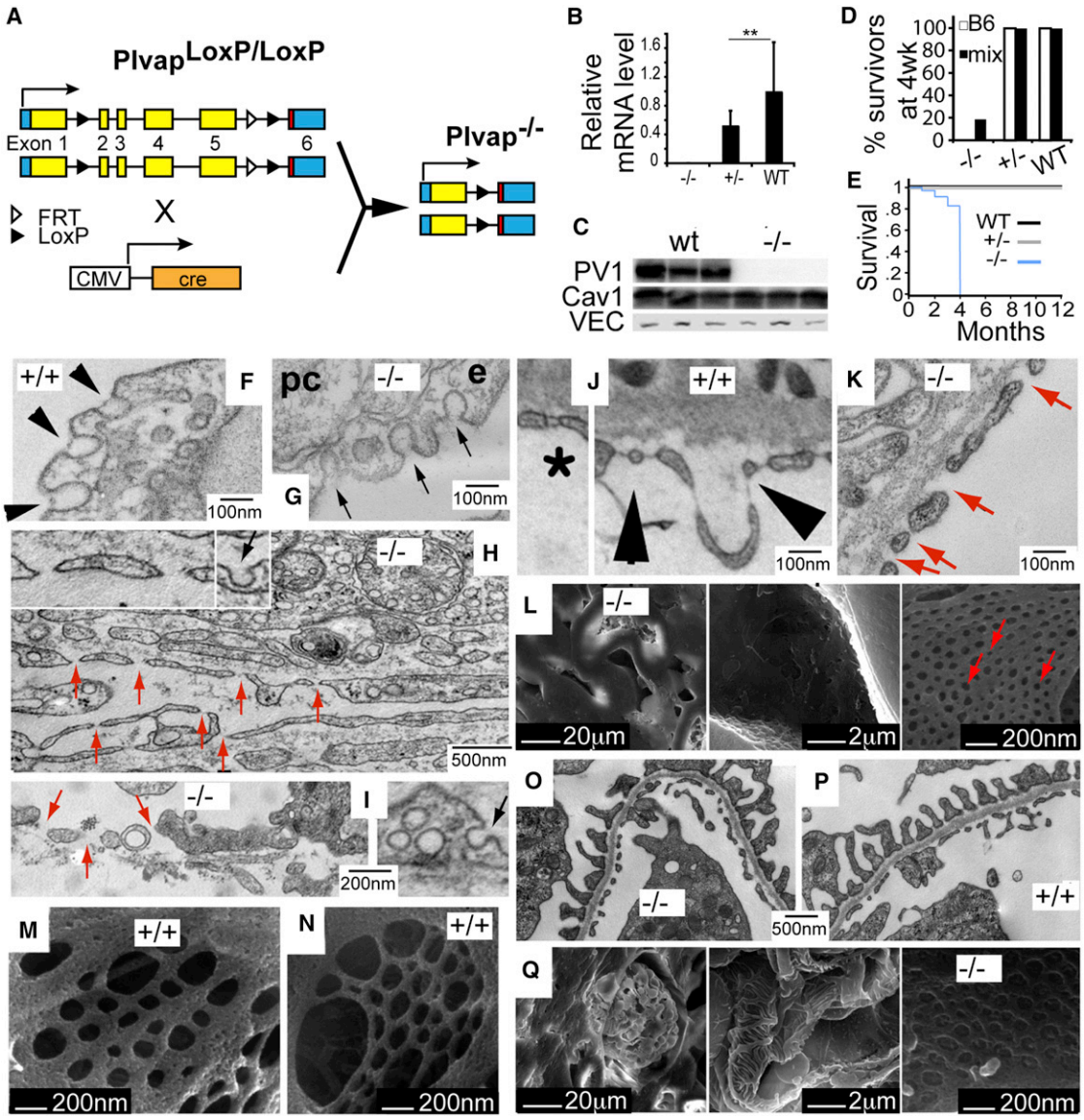

Figure 1. Lack of PV1 Results in Absence of Endothelial Diaphragms and Decreased Survival

(A) Endogenous *PV1* alleles deletion in all cell types via CMV-cre expression.

(B) PV1 mRNA levels in the liver of WT, $PV1^{+/-}$, and $PV1^{-/-}$ mice (n > 4, SD, **p < 0.01).

(C) PV1, Cav1, and VE Cadherin protein levels shown by western blotting of lung tissue from $PV1^{-/-}$ mice and controls.

(D) Mouse survival at 28 days expressed as a percentage of the expected numbers (calculated assuming a Mendelian distribution of offspring genotypes) of the indicated genotypes on either C57Bl/6 (white bars) or C57Bl/6-Balb/c-129Sv/J mixed background (solid bars) ($p < 0.01$, χ^2).

(E) Kaplan-Meier analysis of the survival rate of the WT (n = 485), $PV1^{+/-}$ (n = 899), and $PV1^{-/-}$ (n = 92) mice on mixed background that survived past 28 days.

(F–Q) Transmission (F–K, O–P) and scanning (L–N, Q) electron micrographs from tissues of WT (+/+) (F, J, M, P) and $PV1^{-/-}$ (−/−) (G–I, K, L, N, O, Q) mice. Transmission EM micrographs are from lung (F and G), adrenal (H), pancreas (I), kidney peritubular (J and K) and glomerular (O and P) ECs. The absence of caveolae SDias (black arrows) and of fenestrae FDias (red arrows) in $PV1^{-/-}$ mice is indicated. Black arrowheads indicate the presence of caveolae SDias (F) and of fenestrae FDias (J) in WT tissues. The asterisk in (J) indicates a TEC with SDias. Scanning electron micrographs of liver sinusoidal fenestrae sieve plates (M and N), or increasing magnification (left to right) of kidney peritubular (L) or kidney glomerular (Q) capillaries. The right panels in (O) and (Q) demonstrate diaphragm less fenestrae at high surface density in $PV1^{-/-}$ mice.

See also Figures S1 and S2.

we conducted morphometric analyses in adult $PV1^{-/-}$ mice of mixed background using both transmission and scanning electron microscopy. Diaphragm presence was determined by a combination of ultrathin sectioning (20–40 nm), specimen tilting, and morphometry. We examined (1) organs with fenestrated capillaries where caveolae, TEC, and fenestrae exhibit diaphragms (i.e., adrenals, choroid plexus, kidney, pituitary, thyroid, intestinal villi, salivary glands, and pancreas), (2) the continuous endothelium of lung capillaries that exhibits only caveolae with SDias, and (3) the two organs with fenestrated endothelia where

Table 1. Electron Microscopic Morphometric Analysis of Presence of Diaphragms in the Capillaries of Different Organs of $PV1^{-/-}$, $PV1^{ECKO\text{-}Tie}$, and $PV1^{ECRC}$ Mice at 4 Weeks of Age

		$PV1^{-/-}$		$PV1^{ECKO\text{-}Tie}$		$PV1^{ECRC}$			
						Fen/TEC %(SD)		Caveolae %(SD)	
Organ	EC Type	Fen/TEC %(SD)	Caveolae %(SD)	Fen/TEC %(SD)	Caveolae %(SD)	Total	w/FDias	Total	w/SDias
Lung	continuous with SDias	ND	78(6)	ND	88(7)	ND	ND	81(4)	61(12)
Adrenals	fenestrated	89(5)	76(16)	ND	ND	93(3)	67(4)	95(1.5)	64(7)
Choroid	fenestrated	96(4)	87(15)	ND	ND	83(14)	64(23)	ND	ND
Kidney PTC	fenestrated	93(4)	85(3)	95(1)	85(3)	92(4)	77(2)	77(12)	63(4)
Intestine	fenestrated	81(3)	69(11)	ND	ND	73(12)	45(13)	ND	ND
Pancreas Exo	fenestrated	91(6)	81(9)	ND	ND	87(4)	59(12)	93(4)	67(8)
Pancreas Endo	fenestrated	88(1)	77(5)	ND	ND	89(10)	74(3)	78(4)	54(14)
Pituitary	fenestrated	86(7)	76(3)	ND	ND	93(4)	73(8)	89(13)	47(12)
Salivary gland	fenestrated	78(9)	65(4)	ND	ND	74(15)	54(17)	64(8)	53(4)
Thyroid	fenestrated	92(2)	84(1.5)	ND	ND	88(13)	62(14)	79(14)	52(19)
Kidney glomerulus	fenestrated: no FDia	95(2)	ND	94(1)	ND	97(2)	5(4)	ND	ND
Liver sinusoids	discontinuous: no FDia	98(1)	ND	97(2)	ND	98(1)	0	89(4)	69(3)

The data are expressed as the average percentage (±SD) of the fenestrae/TEC and caveolae allowing clear identification of the presence or absence of the diaphragms. Fen/TEC, fenestrae and TEC profiles; ND, not determined.

PV1 and diaphragms are normally absent (kidney glomerular and liver sinusoidal capillaries).

Caveolae diaphragms were also absent in $PV1^{-/-}$ capillaries from lung (Figure 1G), adrenals (Figure 1H), pancreas (Figure 1I), pituitary, thyroid, kidney, intestinal villi, and liver (data not shown), as compared to wild-type (WT) exemplified for the lung (Figure 1F). In lungs, the surface density of EC caveolae (data not shown) and the protein levels of its structural component caveolin 1 (Figure 1C) were unchanged in $PV1^{-/-}$ mice by comparison to WT and $PV1^{+/-}$ mice (data not shown). The levels of VE Cadherin were also similar (Figure 1C) suggesting a similar number of vessels.

In control mice, diaphragms were observed in fenestrae and TECs of all fenestrated capillaries examined, as exemplified by kidney peritubular capillaries (Figure 1J). Such diaphragms were absent in the corresponding $PV1^{-/-}$ capillaries (Table 1). Instead, only open conduits/pores in the size range of fenestrae and TECs (~50–120 nm), lacking any electron opaque structure indicative of the diaphragms, were found. Figure 1 illustrates the findings in $PV1^{-/-}$ capillaries from adrenals (Figure 1H), pancreas (Figure 1I), intestine (Figure S2Ba), choroid plexus (Figure S2Bb), pituitary (Figure S2Bc), thyroid (Figure S2Bd), and kidney peritubular capillaries (Figures 1J, 1K, and S2Be). Without diaphragms, it was not possible to reliably discriminate if these pores were fenestrae or TECs. However, the $PV1^{-/-}$ pore surface density (3.87 ± 0.54 SD) was comparable to the aggregated fenestrae/TEC density in WT (4.11 ± 0.36 SD) peritubular capillaries of kidney (Figure 1L). Of minor note, fenestral pores in $PV1^{-/-}$ mice exhibited a larger variation of diameter (Figure 1L, right panel).

In kidney glomerular and liver sinusoidal capillaries, mature fenestrae without FDias are developmentally preceded by PV1-positive fenestrae with FDias (Bankston and Pino, 1980; Ichimura et al., 2008; Wisse, 1970). As demonstrated by the normal fenestrae morphology in sinusoidal (Figures 1M and 1N) and glomerular (Figures 1O–1Q) ECs in $PV1^{-/-}$ mice when compared to WT, PV1 is not involved, even transiently, in the formation of mature fenestrae in these vascular segments.

In conclusion, PV1 is necessary for the in vivo formation of diaphragms but is not required for the formation of caveolae or of fenestrae/TEC pores.

Endothelial-Specific Loss of PV1 Phenocopies PV1 Germline Deletion

To define PV1 functions in ECs and evaluate potential roles in nonendothelial cell types, we generated PV1 cell-type-specific knockout mice and compared them to $PV1^{-/-}$ animals. $PV1^{L/L}$ mice were bred with *Tie2-cre* and *VEC-cre* transgenic mouse lines, generating $PV1^{ECKO\text{-}Tie2}$ and $PV1^{ECKO\text{-}VEC}$ mice, respectively (Figure 2A; Table 2), that target both endothelial and hematopoietic cell compartments during embryogenesis. To discriminate between the impacts of PV1 absence in the endothelial compartment versus hematopoietic compartment, $PV1^{L/L}$ mice were also crossed with *Vav1-cre* mice (Stadtfeld and Graf, 2005), which express cre exclusively in the hematopoietic compartment ($PV1^{HCKO\text{-}Vav}$) (Figure 2A; Table 2).

$PV1^{ECKO\text{-}Tie2}$ and $PV1^{ECKO\text{-}VEC}$ exhibited a PV1 deletion efficiency >95% (Figure S2A) and ~70%–90% (data not shown), respectively, consistent with previous reports (Chen et al., 2009). $PV1^{HCKO\text{-}Vav}$ mice exhibited ~100% deletion in the hematopoietic cells in blood, skin (tail), peritoneal lavage, and spleen (Figure S2B). Deletion in the tail (Figure S2B) was negligible, consistent with the hematopoietic lineage-specific activity of the Vav1 promoter. At the protein level, PV1 levels were drastically reduced in the lungs of $PV1^{ECKO\text{-}Tie2}$ (Figure 2B) and $PV1^{ECKO\text{-}VEC}$ (data not shown) mice, whereas normal in $PV1^{HCKO\text{-}Vav}$ (Figure 2C), as compared to littermate controls.

The deletion of *Pvlap* in endothelial and hematopoietic cells lineages in both $PV1^{ECKO\text{-}Tie2}$ and $PV1^{ECKO\text{-}VEC}$ mice fully phenocopied $PV1^{-/-}$ mice with respect to survival: on pure C57Bl/6J background there were no survivors after P2, whereas on hybrid C57Bl/6J;129Sv/J (87.5%; 12.5%) backgrounds,

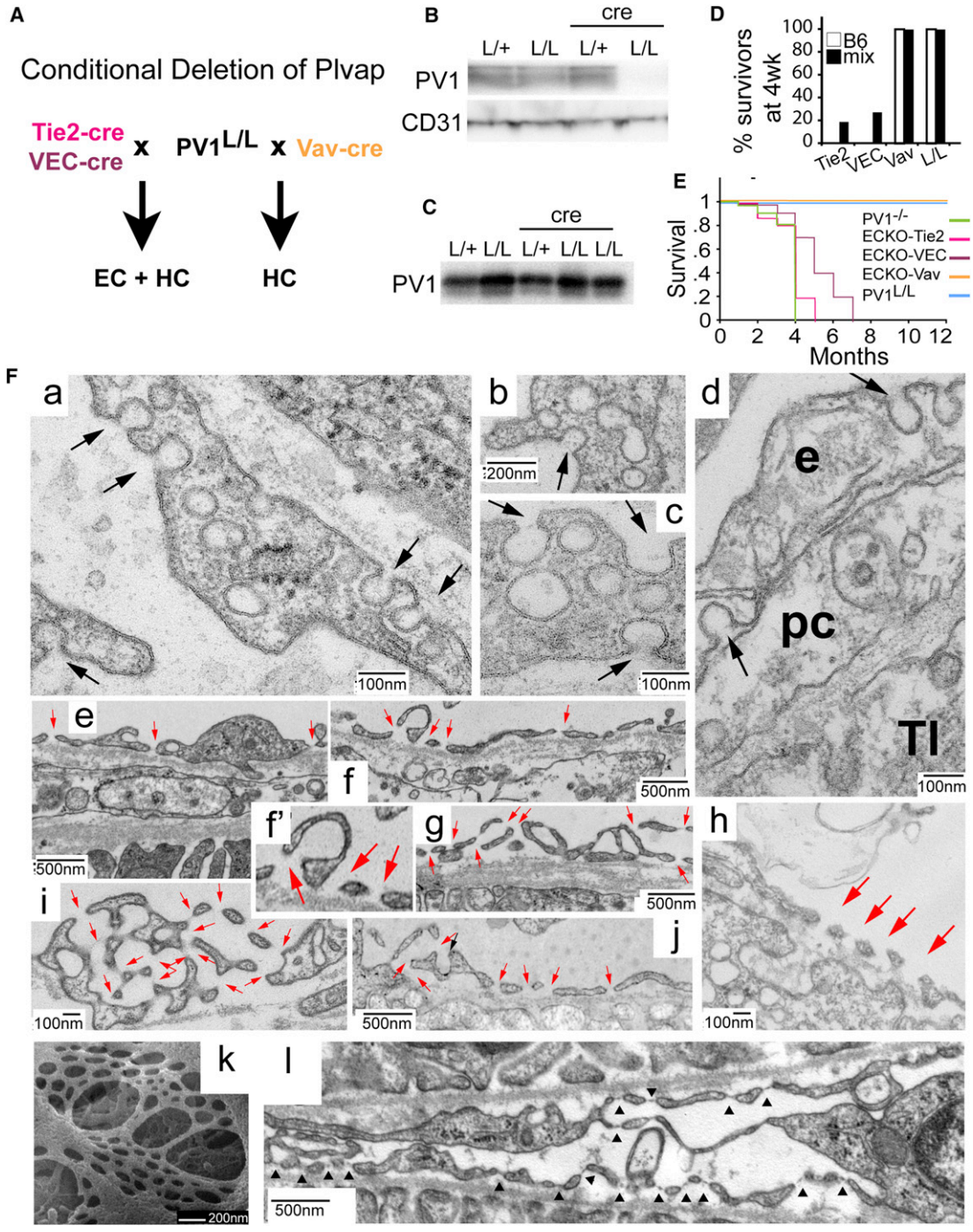

Figure 2. Deletion of PV1 in Endothelial Cells but Not Hematopoietic Cells Phenocopies the Full PV1 Knockout

(A) Schematic of targeted deletion of *PV1* gene in both endothelial and hematopoietic compartments via Tie2-cre and VE Cadherin-cre, and in the hematopoietic compartment only using Vav1-cre. EC, endothelial cells; HC, hematopoietic cells.

(B and C) Western blotting of total lung membranes from $PV1^{ECKO\text{-}Tie2}$ (B) and $PV1^{HCKO\text{-}Vav}$ mice (C) and controls with anti-PV1 antibodies.

(D) Mouse survival at 28 days expressed as a percentage of the expected numbers (calculated assuming a Mendelian distribution of offspring genotypes) of the indicated genotypes on either C57Bl/6 (white bars) or C57Bl/6-129Sv/J mixed background (solid bars) ($p < 0.01$, χ^2).

(E) Kaplan-Meier analysis of the survival rate of $PV1^{L/L}$ (n = 274), $PV1^{ECKO\text{-}VEC}$ (n = 36), $PV1^{ECKO\text{-}Tie2}$ (n = 79), and $PV1^{HCKO\text{-}Vav}$ (n = 22) on C57Bl/6-129Sv/J mixed background that survived past 28 days. $PV1^{-/-}$ (n = 92) mice were also plotted as reference.

(F) Electron micrographs demonstrating the absence of diaphragms in $PV1^{ECKO\text{-}Tie2}$ (a, d–f, f′, i–k) and $PV1^{ECKO\text{-}VEC}$ (b, c, g, h) mice (arrows) and their presence in the $PV1^{HCKO\text{-}Vav1}$ (l) mice (arrowheads). Images are from pancreas (a and i), intestine (b), kidney (c, e–g, l), lung (d), adrenals (h and j), and liver (k). k, scanning electron micrograph.

See also Figure S3.

Table 2. Mouse Lines Generated to Study PV1 Function

Name	Genotype	Background	Tissue Expression	Survival
$PV1^{-/-}$	$PV1^{L/L}$;CMV-Cre	C57BL/6	all tissues	0% by P2
$PV1^{-/-}$	$PV1^{L/L}$;CMV-Cre	BalbC,BL/6,129	all tissues	20% up to 3–4 months
$PV1^{ECKO-VEC}$	$PV1^{L/L}$;VEC-Cre	C57BL/6	EC, HC	0% by P2
$PV1^{ECKO-VEC}$	$PV1^{L/L}$;VEC-Cre	BL/6,129	EC, HC	20%–30% up to 6–7 months
$PV1^{ECKO-Tie2}$	$PV1^{L/L}$;Tie2-Cre	C57BL/6	EC, HC	0% by P2
$PV1^{ECKO-Tie2}$	$PV1^{L/L}$;Tie2-Cre	BL/6,129	EC, HC	20%–30% up to 3–4 months
$PV1^{HCKO-Vav}$	$PV1^{L/L}$;Vav1-Cre	C57BL/6	HC	no phenotype, normal life span
$PV1^{HCKO-Vav}$	$PV1^{L/L}$;Vav1-Cre	BL/6,129	HC	no phenotype, normal life span
VEC-PV1HA	VEC-PV1HA	C57BL/6	EC	no phenotype, normal life span
$PV1^{ECRC}$	$PV1^{-/-}$;VEC-PV1HA	BalbC,BL/6,129	EC	60% up to 18 months

~20%–30% of the expected frequency of each mouse line survived to 3–4 ($PV1^{ECKO-Tie2}$) or 6–7 ($PV1^{ECKO-VEC}$) months (Figures 2D and 2E; Table 2). In contrast, no mortality was observed in $PV1^{HCKO-Vav}$ mice (Figures 2D and 2E). As observed in $PV1^{-/-}$ mice, $PV1^{ECKO-VEC}$ and $PV1^{ECKO-Tie2}$ but not $PV1^{HCKO-Vav}$ mice displayed growth retardation (Figure S2C) with normal organ morphology and histology, reduced pancreas size, and white fat tissue deposits and ascites formation (data not shown).

As observed in $PV1^{-/-}$ mice, both $PV1^{ECKO-Tie2}$ and $PV1^{ECKO-VEC}$ mice lacked diaphragms in endothelial fenestrae, TECs, and caveolae in pancreas (Figures 2Fa and 2Fi), intestine (Figure 2Fb), kidney (Figures 2Fc and 2Fe–2Fg), lung (Figure 2Fd), and adrenals (Figures 2Fh and 2Fj) whereas diaphragms were not affected in the $PV1^{HCKO-Vav}$ mice (Figure 2Fl). These data were confirmed by formal morphometric analysis that was carried out only in kidneys and lungs of $PV1^{ECKO-Tie2}$ mice (Table 1). $PV1^{ECKO-Tie2}$ liver fenestrae morphology (Figure 2Fk) was indistinguishable from WT (Figure 1M).

Therefore, PV1 expression in the endothelial, but not hematopoietic, cells is essential for mouse survival and the cellular and gross phenotype observed in $PV1^{-/-}$ mice stems from loss of PV1 in ECs.

Loss of Endothelial PV1 and Diaphragms Results in Disrupted Blood Composition

The absence of diaphragms should result in leakage of all plasma components with molecular diameters between 6 and 30 nm, representing the interval between the upper pore sizes determined for fenestrated capillaries and their basement membranes respectively (Sarin, 2010). This would encompass all plasma proteins except those that occur in extremely large complexes or lipoprotein particles. Conversely, plasma electrolytes should be relatively unaffected.

Indeed $PV1^{-/-}$ mice, versus control littermates, showed a sharp decrease in total plasma protein, albumin, and albumin/globulin ratio (Figures 3A–3C) associated with minimal electrolyte imbalance featuring a lower calcium concentration (Table S1). Hypoproteinemia developed progressively postnatally with plasma protein levels of $PV1^{-/-}$ mice, compared to control WT and $PV1^{+/-}$ littermates, minimally lower at birth (data not shown), 30%–40% reduced after 1 week, 50%–70% reduced after 4 weeks, and continuing to fall with age (Figures 3A–3C). The altered plasma composition was clearly due to PV1 loss in ECs, as both $PV1^{ECKO-Tie2}$ (Figure 3D) and $PV1^{ECKO-VEC}$ (data not shown) mice exhibited similar levels of hypoproteinemia, whereas $PV1^{HCKO-Vav}$ mice showed no changes in plasma protein levels (data not shown).

SDS-protein acrylamide gel electrophoresis of plasma showed that hypoproteinemia in $PV1^{-/-}$ and $PV1^{ECKO-Tie2}$ mice affected most classes of serum proteins except for proteins larger than 200 kDa, which did not decrease with age (Figure 3E). Similarly, serum protein agarose gel electrophoresis showed that plasma from $PV1^{-/-}$, $PV1^{ECKO-Tie2}$, and $PV1^{ECKO-VEC}$ mice had relative decreases in albumin and β globulin fractions, and a large relative increase in the α globulin fractions (Figure 3F), also demonstrated by densitometry (Figure S3A). The α globulin fractions include some of the largest circulating proteins such as α2 macroglobulin (950 kDa), haptoglobin, pentameric IgM (900 kDa), ceruloplasmin (135 kDa), and ApoB apolipoproteins (250 kDa and 500 kDa), also suggesting that mostly lower molecular weight proteins contribute to hypoproteinemia. A prominent loss of smaller proteins was clearly demonstrated by analysis of protein composition of the ascites fluid formed in both $PV1^{-/-}$ and $PV1^{ECKO}$ mice, which contained albumin and β globulins at the same level with blood plasma but had sharply diminished α fractions (Figure 3F). Combined, these data suggest that PV1 endothelial deficiency leads to "sieving hypoproteinemia," characteristic of hypoproteinemia due to protein loss (i.e., protein losing enteropathy or nephropathy), in which "smaller" plasma proteins preferentially disappear from the plasma.

Major blood plasma proteins are produced in the liver, except for the immunoglobulins (Ig), which are produced by immune cells. Absolute plasma levels of IgA (Figure 3G), IgM (Figure 3H), and IgG (data not shown) were reduced in 4-week-old $PV1^{-/-}$ as compared to WT and $PV1^{+/-}$ littermates. Thus, hypoproteinemia affected levels of proteins produced both in the liver and the immune system.

Other possible causes of hypoproteinemia include decreased production (i.e., due to liver dysfunction, malnutrition, or amino acid malabsorption), increased catabolism or protein loss (due to protein losing enteropathy or nephropathy). The Ig reduction was not due to an intrinsic defect in plasma cells, as isolated $PV1^{-/-}$ plasma cells were perfectly able to produce Ig in vitro, as determined by ELISPOT (data not shown). To determine whether liver function was impaired, we carried out liver function

tests of plasma (e.g., plasma liver enzymes, bilirubin, IgA). *PV1*$^{-/-}$ and *PV1*^{ECKO} mice and their control littermates exhibited similar liver enzymes (AST, ALT, ALP; when standardized to total protein), bilirubin (both direct and indirect) levels (Table S1) and low IgA levels (Figure 3G). Liver production of mRNAs for major plasma proteins (albumin, transferrin, fibrinogen) was found to be higher in *PV1*$^{-/-}$ mice (Figure S3B). These results argue against impaired liver function in *PV1*$^{-/-}$ mice. We were also able to exclude food intake and malabsorption due to pancreatic dysfunction as causes of hypoproteinemia (R.V.S., unpublished data).

Although the observed sieving effect in plasma protein composition suggested the possibility of a nephropathy, *PV1*$^{-/-}$ and PV1^{ECKO} mice at different ages exhibited normal kidney histology (Figures S2A and S3D) and unaltered glomerular ultrastructure (Figures 1O and 1Q). No protein was found in the urine of *PV1*$^{-/-}$ mice between birth and 12 weeks of age. Blood urea nitrogen (Figure S3C) and creatinine levels (Table S1), as well as urinalysis tests on random or 24 hr urine were also normal. Thus, endothelial loss of PV1 does not impair kidney function and does not enhance protein catabolism.

Based on published literature, the gradual decrease in plasma protein should be followed by a certain degree of hypertriglyceridemia due to decreased lipoprotein lipase activity in peripheral tissues and decreased consumption of dietary triglyceride-rich lipoprotein particles such as chylomicron remnants (Shearer and Kaysen, 2006; Yoshino et al., 1993). Moreover, because the particle size of >200 nm is much larger than fenestrae/TEC pores, chylomicron apolipoproteins such as ApoB48 should be spared from plasma protein loss exhibited by *PV1*$^{-/-}$ mice, further demonstrating the sieving. Consistent with these predictions, plasma lipids were normal in postnatal *PV1*$^{-/-}$ mice up to 2 weeks of age (data not shown)—a period of time during which hypoproteinemia first developed. After 2 weeks, PV1$^{-/-}$ plasma showed marked lipid accumulation as shown by its milky aspect (Figure 3I) and by electron microscopy (Figure 3J). The severity of lipid accumulation gradually increased with age, initially confined to the plasma by 4 weeks of age (Figure 3J, left), accompanied by xanthoma (lipid-containing white deposits) on the surface of the heart and liver after 8 weeks (Figure S3E) and later (10–12 weeks) perivascular lipid deposits were formed (Figure 3J, right); after 8 weeks in several tissues lipids were seen engorging the capillaries (Figures 3J, middle, and S3F).

Consistent with these observations, direct lipid measurements in lithium heparin plasma or in serum from *PV1*$^{-/-}$ and control littermates at 4 weeks of age showed severe (10- to 30-fold) increase in plasma triglycerides (TG) (1,500–2,000 mg/dl) and moderately increased total cholesterol (CHOL) (175–250 mg/dl) with significantly decreased HDL cholesterol fraction (HDLc) (20–60 mg/dl) in *PV1*$^{-/-}$ mice (Table S1). Plasma TG levels further increased 30- to 100-fold (up to 5,000–6,000 mg/dl) from 4- to 8-week-old (Figures 3K and 3L) both in *PV1*$^{-/-}$ and *PV1*^{ECKO} mice followed by a slower gradual increase until death at 12–14 weeks (data not shown). In contrast, the elevated total CHOL and reduced HDLc fractions detected in *PV1*$^{-/-}$ and *PV1*^{ECKO} plasma did not vary considerably with time (Figures 3K and 3L). Only extended (24 hr) fasting led to a slow plasma TG level decrease to ~300 mg/dl (Figure 3M), suggesting that slow TG hydrolysis from the lipoprotein particles is one of the probable causes of hypertriglyceridemia. Fasting did not affect CHOL or HDLc levels (Figure 3M). *PV1*^{HCKO} and PV1$^{+/-}$ mice had normal lipid levels (Figure 3I; Table S1).

TGs normally occur in chylomicrons, chylomicrons remnants (CMR), and very low-density lipoproteins (VLDL). *PV1*$^{-/-}$ mice exhibited a dramatic increase in CMR/VLDL as revealed by TEM analysis of the lumen of blood vessels (Figure 3I) and by gel filtration FPLC of plasma samples, showing that CMRs/VLDLs contained the bulk of TG and CHOL (Figure 3N). This identification was further supported by increased ApoB apolipoproteins in the plasma and FPLC fractions (Figures 3N and 3P). There was a dramatic increase of ApoB48 lipoprotein over the ApoB100 (Figures 3O and 3P) suggesting a dietary/intestinal origin for these particles. The intestine is able to produce chylomicrons (Figure S3F). Liver overproduction of VLDL seemed unlikely, based on ApoB and fatty acid synthase mRNA levels being normal (Figure S3G).

Combined these data demonstrate that diaphragm deletion leads to sieving hypoproteinemia, hypertriglyceridemia, and increased plasma concentration of chylomicron remnants.

Lack of Endothelial PV1 Compromises Endothelial Barrier Function to Proteins in Fenestrated Vessels

At 3–4 weeks, *PV1*$^{-/-}$ organs provided with fenestrated vessels (e.g., intestine, kidney, and pancreas) showed signs of edema, whereas heart, liver, brain, and spleen did not show significant changes (Figure 4A), as assessed by wet/dry organ weight ratio. Histologically, intestinal villi were distended with protein-containing material accumulating between the enterocytes and stroma (Figure 4B). ECs did not surround this material, which persisted even after 24 hr starvation and did not stain with lipid probes such as Oil RedO (data not shown), ruling out the possibility that these spaces were lipid-containing distended lymphatics/lacteals. The absence of an inflammatory infiltrate in the intestine (Figure 4B) and any other organs (Figure S2A) showed that edema was not a consequence of inflammation. Altogether, these results strongly suggest that the absence of diaphragms in *PV1*$^{-/-}$ mice produces a leaky fenestrated endothelium.

Plasma proteins leakage into the interstitial space was also examined using the Evans Blue (EB) dye extravasation assay (Bates, 2010). EB binds tightly to plasma proteins (especially albumin) and is normally retained in the vascular space, its extravasation demonstrating protein leakage into the interstitial space. *PV1*$^{-/-}$ mice being severely hypoproteinemic, EB was prebound to purified mouse serum albumin before administration and tissues were harvested after 5 and 15 min, when there is very little EB-albumin extravasation in WT organs. EB-albumin extravasation was dramatically increased at 15 min in *PV1*$^{-/-}$ and *PV1*^{ECKO} organs with fenestrated ECs (e.g., intestine, pancreas, and kidney), in 4-week-old (Figure 4C), and 8-week-old (Figure 4D) mice. Consistent with histological findings, the intestine displayed the highest rate of EB leakage out of its capillaries (Figures 4C–4E). Minimal increase in EB extravasation was observed in the *PV1*$^{-/-}$ lungs (continuous endothelium expressing PV1 and SDias) (Figure 4C, right) or heart (continuous endothelium lacking PV1/diaphragms) (Figures 4C and 4D) but no change was detected in the liver (fenestrated endothelium without FDias but expressing PV1 in SDias) (Figures 4C and 4D).

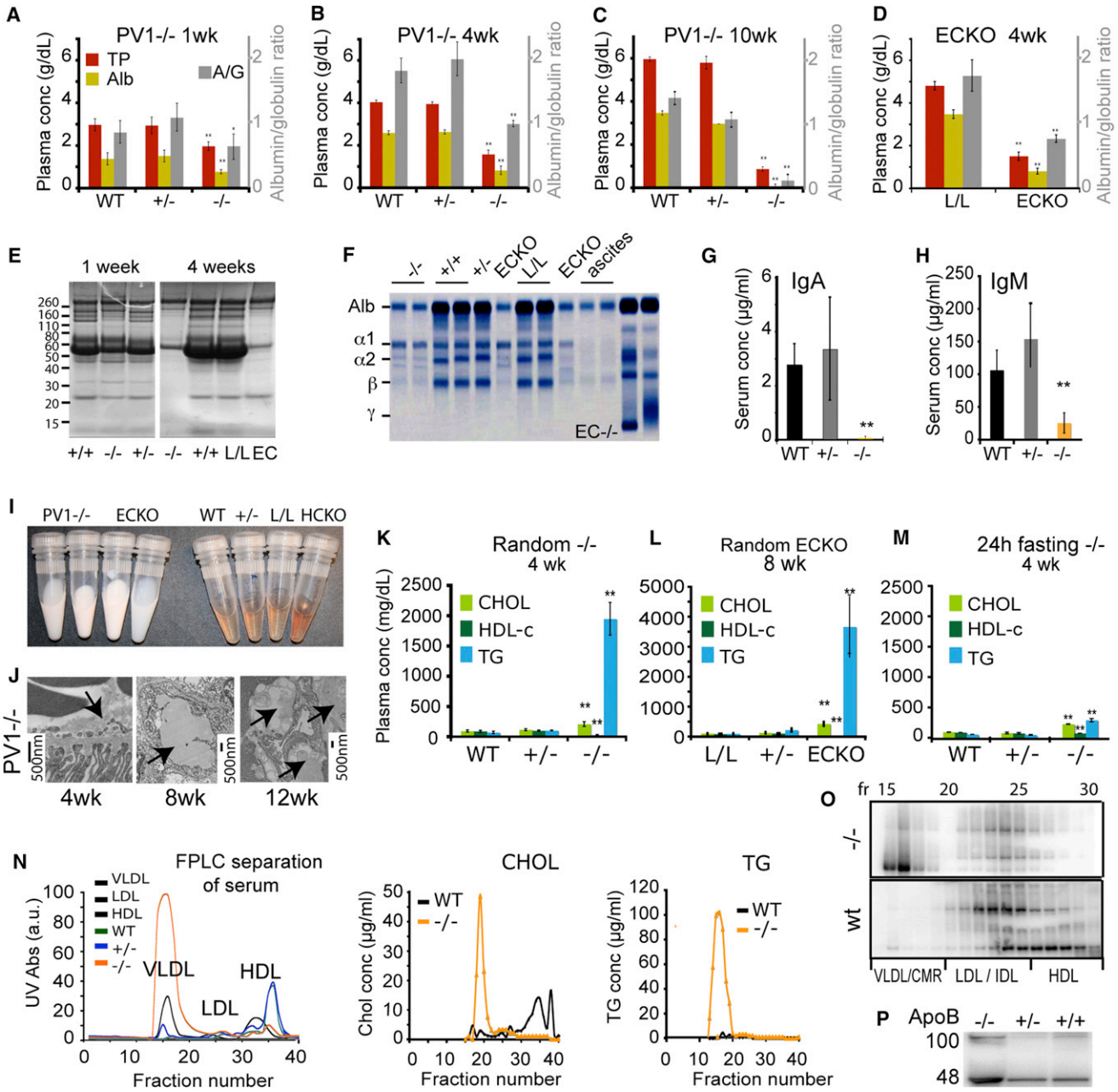

Figure 3. PV1$^{-/-}$ Mice Gradually Develop a Severe Hypoproteinemia and Hypertriglyceridemia

(A–D) Total plasma protein (TP), albumin (Alb) levels, and albumin/globulin ratio (A/G) in nonfasted 1- and 4-week-old (A and B), 24 hr fasted 10-week-old (C) *PV1*$^{-/-}$ mice, and 4-week-old *PV1*$^{ECKO\text{-}Tie2}$ mice (D) with control littermates (n > 5, *p < 0.05, **p < 0.01).

(E) Coomassie blue staining of a 7% SDS PAGE of equal volumes (1 μl) of blood plasma collected from 1-week-old (left) and 4-week-old (right) PV1$^{-/-}$, PV1$^{ECKO\text{-}Tie2}$, and control mice, as indicated.

(F) Equal volumes of serum or ascites fluid from 4-week-old *PV1*$^{-/-}$, WT, *PV1*$^{+/-}$, *PV1*$^{ECKO\text{-}Tie2}$, *PV1*$^{L/+}$, *PV1*$^{L/L}$, and *PV1*$^{ECKO\text{-}VEC}$ mice were subjected to agarose gel protein electrophoresis. Note that the ascites sample came from the *PV1*$^{-/-}$ and *PV1*$^{ECKO\text{-}Tie2}$ mice whose serum is loaded on lanes 1 and 6 from left, respectively. Last two lanes on the right are reference human serum samples.

(G and H) Immunoglobulin A (IgA) and M (IgM) plasma levels in 4-week-old *PV1*$^{-/-}$ versus control mice (n > 4–6, **p < 0.01).

(I) Lithium heparin plasma obtained from *PV1*$^{-/-}$ or *PV1*^{ECKO} mice (left) has a lipid-rich, milky appearance as compared to plasma of WT, *PV1*$^{+/-}$, *PV1*$^{L/L}$, or *PV1*^{HCKO} mice (right).

(J) Electron micrographs showing the presence of lipophilic lipid particles (arrow) in the plasma of kidney peritubular capillary (left) of a 28-day-old *PV1*$^{-/-}$ mouse. At 8 weeks of age lipids (asterisk) in the plasma may coalesce and fully plug capillaries (middle). At 10–12 weeks (right) lipid cuffs (asterisks) surround capillaries in many organs.

(K–M) Plasma lipid profiles in 4-week-old *PV1*$^{-/-}$ (K), 8-week-old *PV1*$^{ECKO\text{-}Tie2}$ (L) mice, and 24 hr fasted 4-week-old *PV1*$^{-/-}$ mice (n > 8 for [K] and n > 5 for [L] and [M], *p < 0.05, **p < 0.01).

EB-albumin extravasation was detected in the ascites in 4-week-old *PV1*$^{-/-}$ mice (Figure 4F). Moreover, EB-albumin was also detected in the lumen of *PV1*$^{-/-}$ small intestine (Figure 4F), clearly demonstrating protein loss through the intestinal mucosa. Similar results were observed in *PV1*$^{ECKO\text{-}Tie2}$ mice (data not shown).

Next, we used fluorescent tracers of various sizes to evaluate the upper pore size (i.e., the diameter of the molecules that do not gain passage across the endothelium) of the fenestrated capillaries in absence of diaphragms. Fluorescent mouse albumin (average molecular radius of 3.6 nm), IgG_2 (5.5 nm), IgM (12 nm), and dextrans of 10 kDa (~2.3 nm) and 70 kDa (5.77 nm) average molecular weight were readily detected in the ascites at 5 and 15 min postadministration, whereas dextran with an average size of 2×10^6 Da (~27.9 nm) leaked much slower (Figure 4G). To corroborate these findings at EM level we introduced in the circulation of *PV1*$^{-/-}$ mice albumin-coated gold nanoparticles of 10, 15, and 25 nm and the site of leakage determined at 5 min of tracer perfusion. We found that, in *PV1*$^{-/-}$ mice, albumin-gold particles of all these sizes are able to exit adrenal capillaries, and the gold particles were clearly associated with diaphragm-less fenestrae/TEC (Figures 4Ha–4He). These data show an increased pore size for *PV1*$^{-/-}$ fenestrated capillaries and identify fenestrae as sites of leakage.

Combined, these data demonstrate that endothelial PV1 is required for maintenance of basal permeability in the adult mouse, particularly in vascular beds with fenestrated capillaries provided with FDias.

Endothelial Reconstitution of PV1 Rescues the *PV1*$^{-/-}$ Phenotype and Restores the Diaphragms of Fenestrae and Caveolae

To demonstrate that the *PV1*$^{-/-}$ phenotype is not due to perturbation of other genes near the *Pvlap* locus, we performed transgenic complementation in which PV1 was reconstituted specifically in ECs of *PV1*$^{-/-}$ mice.

Having previously shown that a HA-tagged PV1 protein behaves as its native counterpart in cultured cells (Stan et al., 2004), we generated mouse lines (*VEC-PV1HA*) expressing PV1-HA under the control of the VE Cadherin promoter and 5′ intronic enhancer (Hisatsune et al., 2005) (Figure 5A). From six founder lines, we selected a line expressing PV1HA in all organs (Figures S4A and S4B) at ~30%–50% of the native PV1 levels in tissues where it is normally expressed such as the lung (Figure 5B). In 4-week-old mice, PV1-HA was detected in ECs of all vessels (i.e., large arteries and veins, capillaries in the heart and muscle, brain vessels, glomerulus) and less in the sinusoids of the liver (Figures S4A and S4B and data not shown). Mosaicism of transgene expression was detected by confocal microscopy (Figure S5A) and 14.6% (±10.3%) of CD31- or VEC (CD144)-positive lung ECs did not express PV1-HA by flow cytometry (data not shown). *VEC-PV1HA*$^{+/tg}$ mice did not exhibit any overt phenotype in terms of survival, fertility, growth, blood composition, or cardiovascular function.

VEC-PV1HA$^{+/tg}$;PV1$^{-/-}$(*PV1*^{ECRC}) mice were generated (Figure 5A) and displayed ~30%–50% reconstitution of PV1HA (Figure 5B) when normalized to the lung endothelial content, as measured by VE cadherin levels, an accepted endothelial marker in the adult (Salomon et al., 1992). These subnative levels of PV1 reconstitution significantly increased *PV1*^{ECRC} mice survival to ~60% of expected Mendelian frequency, on a mixed background (Figure 5C). Moreover, 100% of the *PV1*^{ECRC} mice that survived to 28 days were alive up to 1 year later (Figure 5D).

Importantly, *PV1*^{ECRC} mice displayed diaphragm restoration in the lung, adrenal, kidney, pancreas, thyroid, and intestine (Figure 5E; Table 1). Consistent with the idea of the mosaicism and hypomorphic PV1 expression (Figure S4A) in kidney peritubular capillaries, there were isolated ECs that did not form diaphragms or express PV1 (Figure S4D). Less than 5% of glomerular capillaries exhibiting fenestrae with diaphragms, and no caveolae diaphragms were detected in the heart (Figure 5Eh) muscle or aorta ECs (data not shown).

PV1^{ECRC} mice had normal growth (Figure 5F), near normal level of plasma proteins (Figure 5G), CHOL, and TGs (Figure 5H), and no edema in organs with fenestrated endothelia (Figure S4C). Thus, re-expression of PV1 in ECs of *PV1*$^{-/-}$ mice restores diaphragm formation and rescues their complex vascular leak syndrome.

DISCUSSION

Here, we demonstrated in vivo the essential role of PV1 in the formation of FDias and SDias on endothelial organelles such as fenestrae, TEC, and caveolae, whereas the lack of expression of PV1 does not affect the formation of these organelles. Most importantly, by enabling the formation of the diaphragms of fenestrae/TEC, PV1 plays a critical role in regulating basal permeability to proteins and the maintenance of blood composition. Removal of the diaphragms resulted in early death of mice caused by severe, noninflammatory protein-losing enteropathy. Thus, the role of PV1-containing diaphragms in regulation of basal permeability is absolutely essential for postnatal survival.

At the ultrastructural/subcellular level, we show that the deletion of PV1 results in complete absence of SDias and FDias in situ, confirming previous in vitro data (Ioannidou et al., 2006; Stan et al., 2004) and further validating our model by which PV1 is necessary for diaphragm formation. Notwithstanding the inherent technical difficulties in ascertaining the loss of diaphragms by electron microscopy (depending on the thickness of the section and on how much of the fenestrae/TEC pore rim was encompassed in the section), we did not find a single

(N) Size exclusion by fast protein liquid chromatography (FPLC) of serum from *PV1*$^{-/-}$ and control littermates. UV absorption profiles of FPLC fractions (left) from PV1$^{-/-}$ (orange), PV1$^{+/-}$ (blue), and WT (green) serum. Elution peaks of human VLDL, LDL, and HDL controls are also shown (black). Average CHOL (middle) and TG (right) concentration in serum FPLC fractions from *PV1*$^{-/-}$ (orange) and control (black) mice. FPLC, fast protein liquid chromatography; HDL, high density lipoprotein; LDL, low density lipoprotein; VLDL, very low density lipoprotein.
(O and P) Western blotting with an ApoB antibody recognizing both ApoB48 and ApoB100 apolipoproteins of (O) serum FPLC fractions and (P) total plasma samples from *PV1*$^{-/-}$ and control mice. All error bars represent SD.
See also Figure S4 and Table S1.

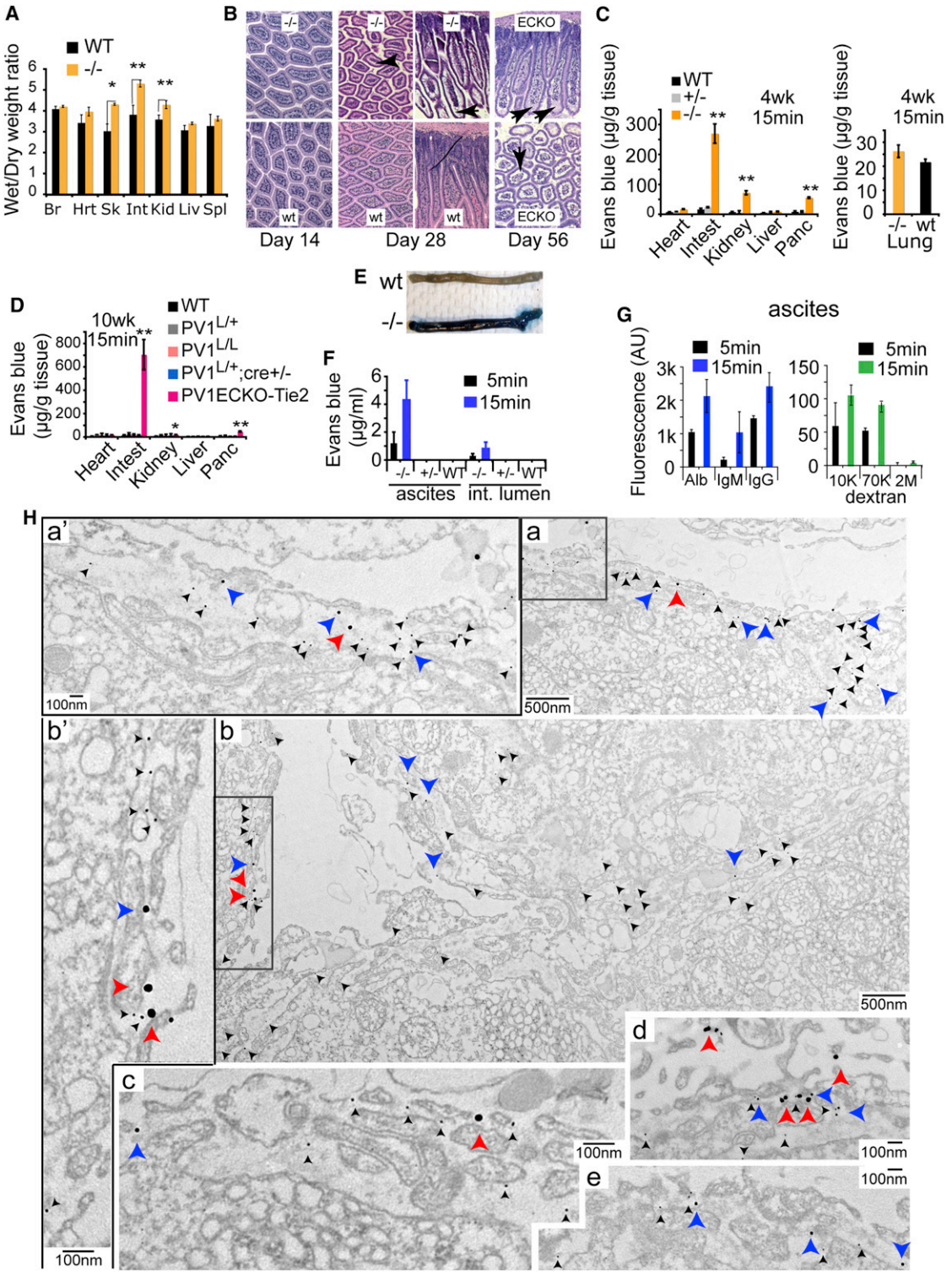

Figure 4. Vascular Leak of Proteins in PV1$^{-/-}$ Organs Provided with Fenestrated Endothelium

(A) Comparison of wet/dry weight ratio of different organs from *PV1*$^{-/-}$ and WT mice at 4 weeks of age.

(B) H&E stained sections of formalin fixed paraffin embedded small intestine (jejenum) of 2-week-old (two left panels), 4-week-old (middle four panels), and 8-week-old mice (right two panels). In the left and middle panels the bottom micrographs demonstrate the intestine from wild-type (WT), whereas the top micrographs show intestine from *PV1*$^{-/-}$ (–/–) mice. Both micrographs on the right demonstrate the intestine from *PV1*$^{ECKO\text{-}Tie2}$ (ECKO) mice in two different cuts (top, section orthogonal to the intestine wall; bottom, section parallel to the intestinal wall through the intestinal villi). In both *PV1*$^{-/-}$ and *PV1*$^{ECKO\text{-}Tie2}$ samples arrows point to edema.

diaphragm in any of the structures we were able to examine in $PV1^{-/-}$ and $PV1^{ECKO\text{-}Tie2}$ mice. The hypomorphic rescue of PV1 in ECs restores all types of diaphragms and TEC. Interestingly, expression of PV1 in vivo restores diaphragms only in the ECs where they natively occur, demonstrating the essential but not sufficient role PV1 in the diaphragms formation.

PV1 is not necessary for the formation of fenestrae/TEC pores and caveolae. Surface density of these organelles is similar in $PV1^{-/-}$ and WT littermates. The only observed difference is in a greater variation in the diameter of fenestrae and TEC in $PV1^{-/-}$ mice. These findings are in agreement with the idea generated decades ago that a possible function of diaphragms was to maintain the size, shape, and distribution of the fenestrae (Clementi and Palade, 1969b), recently bolstered by in vitro studies (Ioannidou et al., 2006). No conduits resembling TEC without diaphragms were found, suggesting either that PV1 is required for TEC pore formation or, more likely, that TEC are precursors of fenestrae and the double diaphragms are required for maintenance of the channel length.

Formation of the diaphragms regulates basal permeability to proteins. Deletion of FDias causes leakage of plasma proteins into the peritoneal cavity and into the interstitium of organs provided with fenestrated capillaries (i.e., intestine, kidney, pancreas) but not in organs with continuous endothelium (heart, muscle, lung) in $PV1^{-/-}$ and $PV1^{ECKO}$ mice. In contrast, the sites where fenestrae have no FDias (i.e., liver sinusoids or glomerulus) do not exhibit changes in permeability. The leakage involves most plasma proteins, up to the size of IgM (molecular radius, 12 nm), or tracers as large as 2×10^6 kDa dextran (molecular radius 27.9 nm), but not the components of the largest lipoprotein particles such as VLDL/chylomicron remnants. We demonstrate that nanoparticles as large as 25 nm are able to exit fenestrated vessels on a very fast timescale (5 min). Although the EM micrographs do not allow dynamic visualization of the site of leakage, the gold particles (especially the larger ones) were found closely associated with clusters of fenestrae/TEC pores, thus bolstering our claims that in absence of diaphragms fenestrae/TEC pores leak plasma molecules with much larger diameter that in WT.

Thus, the FDias act as size selective molecular sieves with a function reminiscent of that of the podocyte slit diaphragms in the mature kidney glomerulus, which have been more intensively studied. Although the molecular architecture is not precisely the same (i.e., spoke and wheel radial versus zipper-like parallel fibrils), both types of diaphragms make use of transmembrane N-linked glycoproteins with large extracellular domains (i.e., PV1 and nephrin) revealing a general building principle of vascular sieves. Although additional proteins (e.g., Neph-1, FAT1) enable the formation of slit diaphragms, the FDia structure might involve other proteins in addition to PV1, which we are actively pursuing.

Lack of caveolar SDias in fenestrated endothelia does not seem to have a role in plasma protein extravasation seen in $PV1^{-/-}$ mice, as no differences in EB extravasation are observed between the lungs of $PV1^{-/-}$ mice and control, where capillaries contain only caveolar SDias. The lack of role of caveolar SDias in basal permeability is also suggested by the fact that permeability to proteins in continuous endothelia where caveolae do (i.e., lung) or do not (i.e., heart, skeletal muscle) have SDias is similar (for review, see Sarin, 2010), or it is enhanced when the SDias are present (King et al., 2004). How much of the increased permeability to proteins in $PV1^{-/-}$ mice is the result of the deletion of diaphragms of fenestrae or those of TEC and whether knocking out PV1 deletes the proteoglycans within fenestrae, is a matter of further study.

Lack of diaphragms resulted in defects in blood composition and protein losing enteropathy causing early death of $PV1^{-/-}$ mice on mixed background. $PV1^{-/-}$ and $PV1^{ECKO}$ (but not $PV1^{HCKO}$) mice have numerous homeostatic defects, which are rescued by the reconstitution of the diaphragms in ECs of $PV1^{ECRC}$ mice, an important confirmation that the defects are directly related to the loss of diaphragms. These defects include significant growth retardation, declining plasma protein levels, increase in TG-rich lipoprotein particles, edema, and ascites formation, consistent with protein calorie malnutrition. The hypoproteinemia is central to the $PV1^{-/-}$ phenotype. Although decreased protein production, enhanced protein catabolism, and protein loss by nephrotic syndrome were ruled out, intestinal loss of protein as a cause of hypoproteinemia was confirmed by permeability studies in $PV1^{-/-}$ and $PV1^{ECKO}$ mice, which demonstrated sharply increased protein extravasation and loss in the intestinal lumen.

The increases in TG-rich lipoprotein particles in $PV1^{-/-}$ mice follow hypoproteinemia, the former being a known sequel of hypoproteinemia in both humans and rodents (Shearer and Kaysen, 2006; Yoshino et al., 1993). However, the severity of plasma TG increases in $PV1^{-/-}$ mice is unusually high and might reflect the magnitude of the protein loss in $PV1^{-/-}$ mice or additional mechanisms by which PV1 regulates TG metabolism. The increase in plasma concentration of ApoB48-containing CMRs with diameters much larger than the diaphragm-less fenestrae pores brings strong support to the idea of an increase in the upper pore size of the capillary wall of the $PV1^{-/-}$ fenestrated vessels. Conversely, the leakage is restricted to probes smaller than the fenestrae pores.

In the light of the gradual character of the changes in $PV1^{-/-}$ and $PV1^{ECKO}$ mice on the mixed 129Sv/J x C57BL/6J background, a plausible scenario unfolds by which the deletion of

(C and D) Retention of Evans Blue (EB) at 15 min following administration of EB-serum albumin in organs of (C) 4-week-old $PV1^{-/-}$ mice and (D) 10-week-old $PV1^{ECKO\text{-}Tie2}$ mice and controls (n = 4, **p < 0.01).

(E) Representative image of duodenum of $PV1^{-/-}$ (up) and WT (down) mice at 15 min post-EB administration.

(F) EB quantification in ascites fluid and intestine lumen of $PV1^{-/-}$ mice at 5 min post-EB administration (n = 4, **p < 0.01).

(G) Measurement of leakage of fluorophore-labeled tracers in the ascites fluid of $PV1^{-/-}$ mice at 5 and 15 min post-EB administration (data expressed as arbitrary fluorescence units) (n > 3, p < 0.01 versus WT).

(H) Representative electron micrographs documenting leakage of serum albumin-gold nanoparticles in the adrenals of $PV1^{-/-}$ mice. Arrowheads indicate the position of 10 nm (black), 15 nm (blue), and 25 nm (red) albumin-gold conjugates after 5 min perfusion of the tracer mixture. (a) and (b) show lower magnification fields with details magnified in (a′) and (b′). (b) A montage of two separate micrographs of adjacent fields. All error bars represent SD.

See also Table S2.

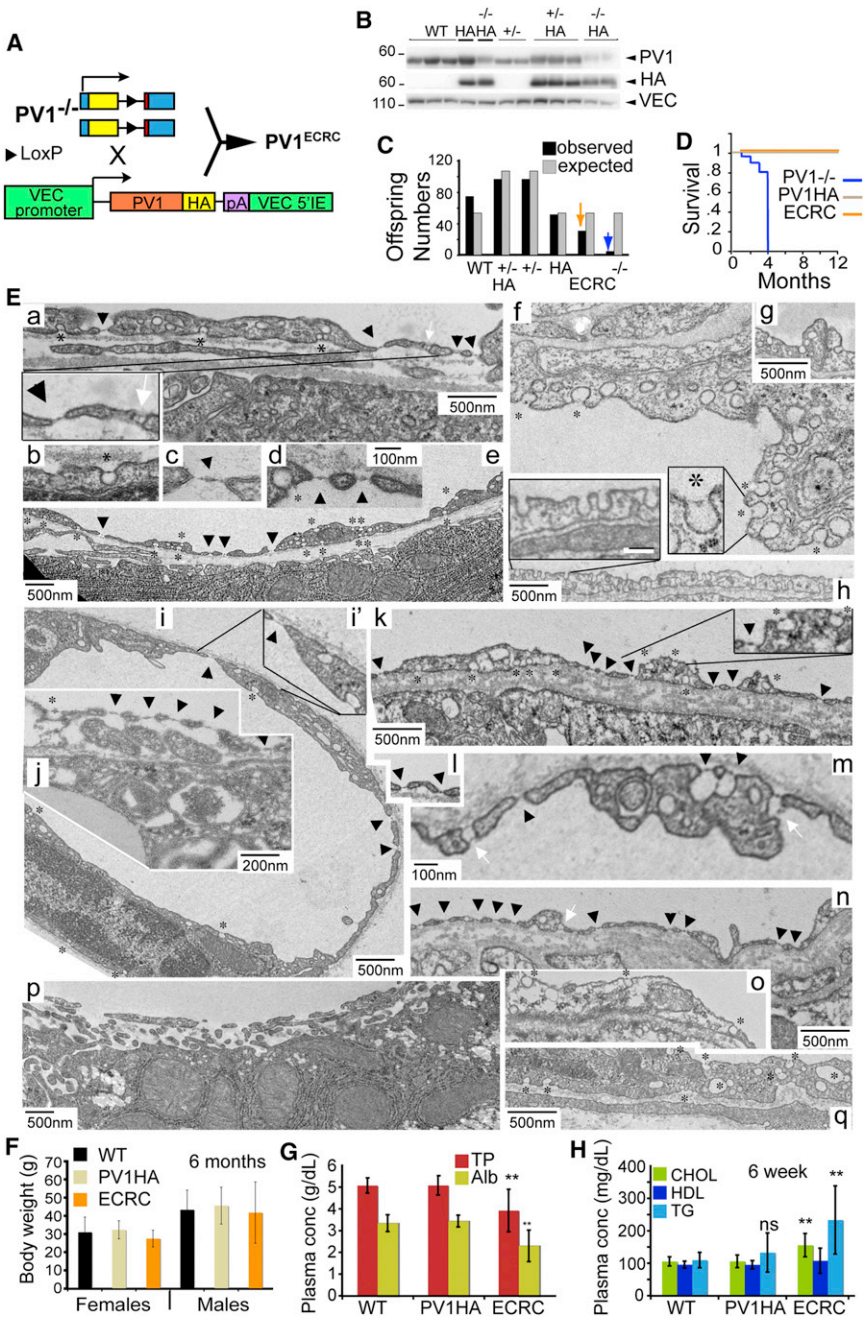

Figure 5. Endothelial-Specific Reconstitution of PV1 Rescues the PV$^{-/-}$ Phenotype

(A) Schematic of endothelial-specific PV1 reconstitution in *PV1^{ECRC}* mice.

(B) Western blotting of equal amounts of lung membrane proteins with anti-PV1, anti-HA, and anti-VE Cadherin antibodies.

(C) Survival of *PV1^{ECRC}* and control genotypes at weaning on a mixed background. The orange and blue arrows highlight the observed differences in of *PV1^{ECRC}* and *PV1$^{-/-}$* offspring numbers, respectively.

(D) Kaplan-Meier analysis of the survival of *PV1^{ECRC}*, *PV1HA*, and *PV1$^{-/-}$* mice that survived past 4 weeks.

(E) Electron micrographs documenting the reconstitution of SDias and FDias in capillary endothelia of *PV1^{ECRC}* mice: kidney (a, a′–c), pancreas (d and e), lung (f and g), heart (h), intestine villus (i and i′), adrenal (j), thyroid (k and l), salivary glands (m), thyroid (n and o) and liver sinusoid (p), and liver centrolobular vein (q). FDias are indicated with arrowheads, SDias of TEC with white arrows whereas SCs of caveolae are indicated by asterisks. Insets show higher magnification of relevant details.

(F and G) Comparison in 6-month-old *PV1^{ECRC}*, *PV1HA* (HA), and WT mice of (F) body weights of the (n > 5, SD), (G) total plasma protein (TP), albumin (Alb) levels, and albumin/globulin ratio (A/G) (n = 4, **p < 0.01).

(H) Plasma total cholesterol (CHOL), HDL cholesterol (HDLc), and triglycerides (TG) concentration of 6-week-old *PV1^{ECRC}* mice. (n = 4, **p < 0.01). All error bars represent SD.

See also Figure S5 and Table S1.

FDias initially cause extravasation of proteins and moderate hypoproteinemia due to the increase in the volume of the compartment to which plasma proteins have access. This volume now includes the intravascular space and the volume of the interstitial space of the organs with fenestrated vessels. Here, the presence of excess protein will cause gradual edema further increasing the protein compartment volume, which may accentuate hypoproteinemia. It is not clear what is the effect of the plasma protein extravasation and edema on the function of most organs with fenestrated vessels. Future experiments using innovative inducible, vascular bed endothelial-specific deletion of PV1 might be able to answer this question. What is clear is that PV1 deletion in mice on mixed background results in an important intestinal edema, which may constitute the basis of the demonstrated intestinal barrier failure and intestinal protein loss. The latter provides a rational explanation for the severe hypoproteinemia and the clear signs of protein calorie malnutrition syndrome resembling kwashiorkor in humans (e.g., growth retardation, severe hypoproteinemia, ascites, hypertriglyceridemia, and lipid deposits), which may be the cause of death in PV1$^{-/-}$ mice.

PV1$^{-/-}$ and *PV1^{ECKO}* (but not *PV1^{HCKO}*) mice exhibited reduced survival with varying severity depending on the background, with the 129/SvJ background mitigating the effects and allowing postnatal life. In all *PV1$^{-/-}$* and *PV1^{ECKO}* mice examined, PV1 and the diaphragms were completely absent; thus the difference in survival was not due to incomplete penetrance of the diaphragm-free phenotype. It is possible that differences in the severity of leakage (in rate and/or components), the impact of the leakage on the function of critical organs (e.g., circumventricular organs and endocrine glands), or effects of PV1 outside fenestrae, might explain the differences between backgrounds. Further studies in mice with

conditional time-resolved deletion/reconstitution of PV1 should elucidate these issues.

While our article was under review, two articles from the same group were published describing the PV1$^{-/-}$ phenotype in mice generated by a targeted trap insertion in intron 1 of *Plvap* locus (Herrnberger et al., 2012a, 2012b). In agreement with our data, Herrnberger et al. (2012a) confirm that PV1 is essential for diaphragm formation in caveolae, fenestrae, and TEC and is not required for the formation of fenestrae pores themselves. They also agree to the premise that PV1$^{-/-}$ mice constitute a good model for studying the role of diaphragms in permeability. Herrnberger et al. (2012a) also observe mouse background-dependent decreased survival, small pancreata and cutaneous hemorrhages in mice that die in utero (which we do not show in this paper) in PV1$^{-/-}$ mice. Interestingly, although we do not observe any statistically relevant changes in surface density of fenestral pores in kidney or qualitative changes in pancreas, Herrnberger et al. (2012a) report a reduction in fenestrae pore numbers in kidney and pancreas although no formal quantification was performed. Another difference, related to the first, is that they did not detect pancreatic edema, which they assessed by qualitative morphology only. These data lead them to speculate that PV1 knockout mouse could have reduced permeability. In contrast, our measurements demonstrate pancreatic, intestinal, kidney, and skin edema with dramatically increased permeability in organs with fenestrated vessels.

These differences could be explained in part by the different mouse genetic backgrounds used in both studies, as we both clearly demonstrated the impact of the background on phenotype severity. The different designs for the null allele (trap insertion in intron 1 and LacZ expression versus deletion of exons 2–5) could also be contributing factors. These differences should inform future studies of PV1 function such as ruling out dominant negative effects of truncation PV1 mutants or the effects of exogenous protein expression.

In summary, deletion of PV1 protein in vivo allowed us to demonstrate that the diaphragms of fenestrae and TEC are critical for the maintenance of endothelial barrier integrity and basal permeability. In the absence of such diaphragms, plasma protein extravasation produces a noninflammatory protein-losing enteropathy resulting in protein calorie malnutrition and ultimately death. Our results and the mouse models we have created provide the foundations for evaluating numerous aspects of basal permeability in fenestrated vascular beds.

EXPERIMENTAL PROCEDURES

Mice

All experiments involving animals have been approved by the Dartmouth College IACUC.

Generation of the PV1$^{L/L}$ Mice

The PV1loxP targeting vector loxP recombination sites in intron 1 and 5, schematized in Figure 1A, was constructed by bacterial artificial chromosome recombination technology. *PV1$^{L/L}$* mice were generated by knockin using homologous recombination in mice (Figures S1C and S1D) at Dartmouth Transgenics Facility.

Targeted PV1 Deletion

PV1$^{L/L}$ mice were bred to *CMV-cre*, *Tie2-cre*, *VEC-cre*, and *Vav-cre* mice, to delete exons 2–5 of the *Plvap* locus in the germline, endothelial and hematopoietic, or hematopoietic only compartments. Genotypes generated are detailed in Table 2.

Generation of VEC-PV1HA Transgenic Mice

The VEC-PV1HA transgenic cassette consisting of the VEC promoter, mouse PV1 fused to 3xHA epitope, SV40 polyA signal sequence, and the 5′ 5 kb of the VE Cadherin intron 1 was used for transgenic mouse generation at Dartmouth Transgenic Facility. *VEC-PV1HA$^{+/-}$* lines were characterized in terms of PV1 expression pattern in blood vessels.

PV1HA Reconstitution in PV1$^{-/-}$ Mice

VEC-PV1HA$^{+/-}$ mice were bred to *PV1$^{+/-}$* to obtain *VEC-PV1HA$^{+/-}$;PV1$^{+/-}$* mice, which were further bred to *PV1$^{+/-}$* to obtain *PV1HA$^{+/-}$*;PV1$^{-/-}$ (*PV1^{ECRC}*) mice.

Survival Analysis

The survival rate of different mouse genotypes mice was calculated from the total observed numbers in each mouse line and assuming a Mendelian distribution of genotypes according to the breeding scheme employed. The statistical significance was calculated using the CHI^2 test.

Transmission Electron Microscopy and Morphometry

Organs were harvested and processed for routine transmission electron microscopy, as described (Tkachenko et al., 2012). Briefly, mice were euthanized with CO_2, and their vasculature immediately flushed free of blood by 5 min perfusion via the left ventricle using the left atrium as an outlet (also ensuring the perfusion of lung vasculature) of Hank's balanced salt solution (HBSS) containing calcium and magnesium (HBSS-CM) followed by 10 min of EM fixative (2% glutaraldehyde, 3% paraformaldehyde, 0.1 M sodium cacodylate, pH 7.2). Tissues were harvested, cut in 1 × 2 mm blocks and fixed further in fresh fixative, rinsed in 0.1 M sodium cacodylate, postfixed in 1% OsO_4 in 0.1 M sodium cacodylate, briefly rinsed, stained en block with Kellenberger's uranyl acetate in water, dehydrated through graded ethanol, and embedded in LX-112 resin (Ladd Research) using propylene oxide for ethanol substitution. Ultrathin sections of 20–40 nm were cut using an ultrasonic diamond knife (Diatome) mounted on grids, stained with uranyl acetate and lead citrate and examined in a Jeol 1010 electron microscope using a bottom mount AMD camera.

For morphometry, pictures of 75 random capillaries (i.e., vessels with <10 μm diameter) were taken from three animals per group (2–5 blocks/animal, 4 animals/genotype) at a magnification of 5,000×. The number of the caveolae, fenestrae, and TEC were expressed as a function of membrane length examined (at least 10 μm in each section). The number of fenestrae/TEC pores per μm linear length of membrane was determined by the method of Milici et al. (1985) (Tkachenko et al., 2012). Student's t test was used to determine statistical significance between different groups.

Scanning Electron Microscopy

Organs were harvested and fixed as above, osmicated, dehydrated in graded ethanol, freeze-fractured in liquid nitrogen, and transferred back in 100% ethanol from where they were subjected to critical point dying using a Samdri 795 device (Tousimis). Dried tissue blocks were mounted on carbon tape-coated 12 mm stubs, osmium coated using an OPC-60N Osmium Plasma Coater Model (SPI) and examined under XL-30 ESEM-FEG field emission gun environmental scanning electron microscope (FEI) operated at 15 kV. Images were collected at 10,000–20,000× magnification.

mRNA Isolation and Real-Time Quantitative PCR

Tissues were collected in RNAlater (QIAGEN) and total RNA isolated using Trizol (Sigma). RNA integrity and purity were determined using Bioanalyzer (Agilent) and NanoDrop (Thermo-Fisher). RNA was reverse transcribed and amplified for quantitative real-time PCR using TaqMan Gene Expression Assays (Applied Biosystems). A list of the Gene Expression Assays used is in the Supplemental Experimental Procedures. The comparative C_T method ($2^{-\Delta\Delta CT}$) of relative quantitation was used to compare different genotypes.

Isolation of Mouse Lung Total Membranes and Blotting

Lung membrane lysates were obtained as described (Stan et al., 1999a). Proteins were separated by SDS- polyacrylamide gel electrophoresis and either silver stained or transferred to PVDF membranes and immunoblotted with various antibodies.

Isolation of Cells for Genotyping or Flow Cytometry

Mouse tissues were flushed free of blood, organs were excised and collagenase treated, and a single cell suspension was prepared and labeled with antibodies as described in the Supplemental Experimental Procedures.

Isolation of Blood Plasma

Mice were euthanized, their thoracic cavity opened, and blood collected from the heart on heparin Microtainer tubes (BD Bioscience). The samples were centrifuged at 6,000 × g for 15 min to obtain platelet-poor plasma.

Isolation of Hematopoietic Cells

Blood was harvested in EDTA-coated Microtainer tubes (BD Biosciences), centrifuged to pellet the blood cells, red blood cells were lysed, white blood cells were collected by centrifugation and used for genomic DNA isolation. Peritoneal cells were harvested by peritoneal lavage using PBS/2% serum albumin/5 mM EDTA and were profiled to determine content of CD45-expressing cells, usually >95%. Spleens were dissociated by mechanical disruption through a 70 μm mesh, yielding <5% nonhematopoietic cells.

Blood plasma measurements (comprehensive metabolic panels, lipid profiles, albumin, and total protein) were done on a chemistry analyzer (Roche MODULAR PPE) by the Dartmouth Department of Pathology Clinical Chemistry Laboratory. Protein subclass determination was done on serum on a Hydrasys-LC system (Sebia). QuantiChrome kits for total protein, albumin, CHOL, and TGs determination were used, as per manufacturer's instructions (BioAssay Systems). Random or fasting venous blood was collected with a heparin-coated capillary tube, and spotted on the strips of an Accu-Check Instant Plus device (Roche) as per manufacturer's instructions.

Serum IgG, IgM, and IgA levels were determined using ELISA kits (ICL), as per manufacturer's instructions.

Plasma lipoprotein fractionation was done by FPLC (Superose 6, GE Healthcare) at a flow rate of 0.25 ml/min, and 0.5-ml fractions were collected.

MRI and fat volume determination were performed on a 7T Varian Unity Inova magnetic resonance spectrometer equipped with a triple axes gradients, as described in the Supplemental Experimental Procedures.

Organ/Body Weight Ratio

Organs were removed, weighed, dried in an oven at 80°C for 7 days, weighed again, and wet/dry weight ratio was calculated.

Histology

Mouse organs were fixed in 10% buffered formalin and embedded in paraffin. For Oil RedO fat content analysis, organs were fixed (24 hr, room temperature [RT]) in methanol-free 4% paraformaldehyde in PBS, followed by cryoembedding in OCT (Tissue-Tek).

Evans Blue Dye Extravasation Assay

Under anesthesia with isoflurane, mice were injected intravenously (i.v.) with 100 μl/20 g body weight of sterile 2% Evans Blue, 6% mouse serum albumin (99.9% pure, MP Bio) in 0.9% saline. To determine Evans Blue extravasation in the organs, the tracer was allowed to circulate for the noted amount of time, when the mice were euthanized and their vasculature perfused (1 ml/min, 10 min, RT) with PBS via the left and right ventricles to remove the intraluminal dye from the systemic and pulmonary circulation, respectively. Organs of interest were harvested, weighed, extracted in formamide, and Evans Blue content calculated as detailed in the Supplemental Experimental Procedures. The Evans Blue content in the peritoneal cavity and intestinal lumen was determined at 5 and 15 min without PBS perfusion ensuring minimal disruption to the circulation.

Leakage of Tracers Directly Labeled with Fluorophores

Under anesthesia with isoflurane, *PV1*$^{-/-}$ mice were injected i.v. with 100 μl/10 g body weight of sterile fluorescent tracer in 0.9% saline. The tracers used were BSA-Alexa647 (250 μM), mouse IgG-Alexa555 (100 μM), mouse IgM-Alexa647, and FITC-dextrans with molecular averages of 10 kDa, 70 kDa, and 2 × 10^6 Da. At the indicated time points, mice were euthanized, ascites fluid collected in *PV1*$^{-/-}$ mice and its fluorescence intensity was determined.

Leakage of Albumin-Gold Nanoparticles

Gold nanoparticles of 10, 15, and 25 nm average diameter (EMS) were separately stabilized by coating with BSA per manufacturer's instructions, collected by ultracentrifugation, and mixed to yield a triple tracer mixture that was adjusted to 1% BSA in 0.9% saline. *PV1*$^{-/-}$ and WT mice (n = 4/group, 4-week-old) were euthanized and their blood was flushed out by perfusion with PBS via the left ventricle, while ligatures were placed on the abdominal aorta above and below the renal arteries and the abdominal aorta was cannulated using a custom-made catheter. The kidneys and adrenals were perfused (0.5 ml/min, 5 min, RT) with triple tracer preparation via abdominal aorta using a nick in the inferior vena cava as an outlet, followed by removal of excess gold particles by perfusion of PBS (0.5 ml/min, 5 min at RT) and EM fixative perfusion (0.5 ml/min, 10 min at RT). Kidneys and adrenals were collected, trimmed into blocks, and processed for LX112 embedding and sectioning, as described above. Ultrathin sections were stained with only uranyl acetate to facilitate gold particle detection.

Morphometric analysis of gold nanoparticle extravasation was carried out on EM micrographs of capillaries (i.e., vessels with diameters of <10 μm) from three mice per genotype. For each capillary profile, the number of gold particles of each size found outside the vessel lumen was determined and expressed as particles per micrometer of membrane length.

Statistical significance was determined by two-tailed Student's t test, ANOVA, or χ^2 test, as appropriate.

SUPPLEMENTAL INFORMATION

Supplemental Information includes five figures, two tables, and Supplemental Experimental Procedures and can be found with this article online at http://dx.doi.org/10.1016/j.devcel.2012.11.003.

ACKNOWLEDGMENTS

This work was supported from NIH grants HL83249, HL092085, RR16437 (PI Green), and GSM funds to R.V.S. We thank J. Chen (UNC Chapel Hill) for help with the *Plvap* targeting construct, N. Speck and M. Chen for VEC-cre, S. Graff for Vav1-cre mice, R. Milne for ApoB antibodies, F. Polito and M. Curtis for plasma measurements, and D. Madden and E. Tkachenko for critically reading the manuscript. R.V.S., D.T., S.J.D., N.C.S., Y.X., M.R.L., C.L.M., M.B., K.V.N., R.E., T.K., S.L.S., K.L.M., and C.C. performed experiments. H.-K.L., A.R.S., A.A.S., and D.S.L. evaluated pathology specimens. P.A.E. provided critical reagents. R.V.S., D.T., S.N.F., R.J.N., C.P.D., B.G., and C.C. designed experiments. R.V.S., N.W.S., and C.C. wrote the paper.

Received: June 11, 2011
Revised: September 7, 2012
Accepted: November 11, 2012
Published online: December 10, 2012

REFERENCES

Aird, W.C. (2007). Phenotypic heterogeneity of the endothelium: I. Structure, function, and mechanisms. Circ. Res. *100*, 158–173.

Bankston, P.W., and Pino, R.M. (1980). The development of the sinusoids of fetal rat liver: morphology of endothelial cells, Kupffer cells, and the transmural migration of blood cells into the sinusoids. Am. J. Anat. *159*, 1–15.

Bates, D.O. (2010). Vascular endothelial growth factors and vascular permeability. Cardiovasc. Res. *87*, 262–271.

Bearer, E.L., and Orci, L. (1985). Endothelial fenestral diaphragms: a quick-freeze, deep-etch study. J. Cell Biol. *100*, 418–428.

Carson-Walter, E.B., Hampton, J., Shue, E., Geynisman, D.M., Pillai, P.K., Sathanoori, R., Madden, S.L., Hamilton, R.L., and Walter, K.A. (2005). Plasmalemmal vesicle associated protein-1 is a novel marker implicated in brain tumor angiogenesis. Clin. Cancer Res. *11*, 7643–7650.

Chen, J., Stahl, A., Krah, N.M., Seaward, M.R., Joyal, J.S., Juan, A.M., Hatton, C.J., Aderman, C.M., Dennison, R.J., Willett, K.L., et al. (2012). Retinal expression of Wnt-pathway mediated genes in low-density lipoprotein receptor-related protein 5 (Lrp5) knockout mice. PLoS ONE *7*, e30203.

Chen, M.J., Yokomizo, T., Zeigler, B.M., Dzierzak, E., and Speck, N.A. (2009). Runx1 is required for the endothelial to haematopoietic cell transition but not thereafter. Nature *457*, 887–891.

Clementi, F., and Palade, G.E. (1969a). Intestinal capillaries. I. Permeability to peroxidase and ferritin. J. Cell Biol. *41*, 33–58.

Clementi, F., and Palade, G.E. (1969b). Intestinal capillaries. II. Structural effects of EDTA and histamine. J. Cell Biol. *42*, 706–714.

Deharvengt, S.J., Tse, D., Sideleva, O., McGarry, C., Gunn, J.R., Longnecker, D.S., Carriere, C., and Stan, R.V. (2012). PV1 down-regulation via shRNA inhibits the growth of pancreatic adenocarcinoma xenografts. J. Cell. Mol. Med. *16*, 2690–2700.

Dvorak, H.F. (2010). Vascular permeability to plasma, plasma proteins, and cells: an update. Curr. Opin. Hematol. *17*, 225–229.

Hallmann, R., Mayer, D.N., Berg, E.L., Broermann, R., and Butcher, E.C. (1995). Novel mouse endothelial cell surface marker is suppressed during differentiation of the blood brain barrier. Dev. Dyn. *202*, 325–332.

Herrnberger, L., Ebner, K., Junglas, B., and Tamm, E.R. (2012a). The role of plasmalemma vesicle-associated protein (PLVAP) in endothelial cells of Schlemm's canal and ocular capillaries. Exp. Eye Res. *105C*, 27–33.

Herrnberger, L., Seitz, R., Kuespert, S., Bösl, M.R., Fuchshofer, R., and Tamm, E.R. (2012b). Lack of endothelial diaphragms in fenestrae and caveolae of mutant Plvap-deficient mice. Histochem. Cell Biol. *138*, 709–724.

Hisatsune, H., Matsumura, K., Ogawa, M., Uemura, A., Kondo, N., Yamashita, J.K., Katsuta, H., Nishikawa, S., Chiba, T., and Nishikawa, S. (2005). High level of endothelial cell-specific gene expression by a combination of the 5′ flanking region and the 5′ half of the first intron of the VE-cadherin gene. Blood *105*, 4657–4663.

Hnasko, R., and Ben-Jonathan, N. (2005). Developmental regulation of PV-1 in rat lung: association with the nuclear envelope and limited colocalization with Cav-1. Am. J. Physiol. Lung Cell. Mol. Physiol. *288*, L275–L284.

Hnasko, R., McFarland, M., and Ben-Jonathan, N. (2002). Distribution and characterization of plasmalemma vesicle protein-1 in rat endocrine glands. J. Endocrinol. *175*, 649–661.

Hnasko, R., Carter, J.M., Medina, F., Frank, P.G., and Lisanti, M.P. (2006a). PV-1 labels trans-cellular openings in mouse endothelial cells and is negatively regulated by VEGF. Cell Cycle *5*, 2021–2028.

Hnasko, R., Frank, P.G., Ben-Jonathan, N., and Lisanti, M.P. (2006b). PV-1 is negatively regulated by VEGF in the lung of caveolin-1, but not caveolin-2, null mice. Cell Cycle *5*, 2012–2020.

Ichimura, K., Stan, R.V., Kurihara, H., and Sakai, T. (2008). Glomerular endothelial cells form diaphragms during development and pathologic conditions. J. Am. Soc. Nephrol. *19*, 1463–1471.

Ioannidou, S., Deinhardt, K., Miotla, J., Bradley, J., Cheung, E., Samuelsson, S., Ng, Y.S., and Shima, D.T. (2006). An in vitro assay reveals a role for the diaphragm protein PV-1 in endothelial fenestra morphogenesis. Proc. Natl. Acad. Sci. USA *103*, 16770–16775.

Keuschnigg, J., Henttinen, T., Auvinen, K., Karikoski, M., Salmi, M., and Jalkanen, S. (2009). The prototype endothelial marker PAL-E is a leukocyte trafficking molecule. Blood *114*, 478–484.

King, J., Hamil, T., Creighton, J., Wu, S., Bhat, P., McDonald, F., and Stevens, T. (2004). Structural and functional characteristics of lung macro- and microvascular endothelial cell phenotypes. Microvasc. Res. *67*, 139–151.

Komarova, Y., and Malik, A.B. (2010). Regulation of endothelial permeability via paracellular and transcellular transport pathways. Annu. Rev. Physiol. *72*, 463–493.

Levick, J.R., and Smaje, L.H. (1987). An analysis of the permeability of a fenestra. Microvasc. Res. *33*, 233–256.

Levick, J.R., and Michel, C.C. (2010). Microvascular fluid exchange and the revised Starling principle. Cardiovasc. Res. *87*, 198–210.

Madden, S.L., Cook, B.P., Nacht, M., Weber, W.D., Callahan, M.R., Jiang, Y., Dufault, M.R., Zhang, X., Zhang, W., Walter-Yohrling, J., et al. (2004). Vascular gene expression in nonneoplastic and malignant brain. Am. J. Pathol. *165*, 601–608.

Milici, A.J., L'Hernault, N., and Palade, G.E. (1985). Surface densities of diaphragmed fenestrae and transendothelial channels in different murine capillary beds. Circ. Res. *56*, 709–717.

Mozer, A.B., Whittemore, S.R., and Benton, R.L. (2010). Spinal microvascular expression of PV-1 is associated with inflammation, perivascular astrocyte loss, and diminished EC glucose transport potential in acute SCI. Curr. Neurovasc. Res. *7*, 238–250.

Niemelä, H., Elima, K., Henttinen, T., Irjala, H., Salmi, M., and Jalkanen, S. (2005). Molecular identification of PAL-E, a widely used endothelial-cell marker. Blood *106*, 3405–3409.

Paes, K.T., Wang, E., Henze, K., Vogel, P., Read, R., Suwanichkul, A., Kirkpatrick, L.L., Potter, D., Newhouse, M.M., and Rice, D.S. (2011). Frizzled 4 is required for retinal angiogenesis and maintenance of the blood-retina barrier. Invest. Ophthalmol. Vis. Sci. *52*, 6452–6461.

Predescu, S.A., Predescu, D.N., and Malik, A.B. (2007). Molecular determinants of endothelial transcytosis and their role in endothelial permeability. Am. J. Physiol. Lung Cell. Mol. Physiol. *293*, L823–L842.

Reeves, W.H., Kanwar, Y.S., and Farquhar, M.G. (1980). Assembly of the glomerular filtration surface. Differentiation of anionic sites in glomerular capillaries of newborn rat kidney. J. Cell Biol. *85*, 735–753.

Rippe, B., Rosengren, B.I., Carlsson, O., and Venturoli, D. (2002). Transendothelial transport: the vesicle controversy. J. Vasc. Res. *39*, 375–390.

Rostgaard, J., and Qvortrup, K. (1997). Electron microscopic demonstrations of filamentous molecular sieve plugs in capillary fenestrae. Microvasc. Res. *53*, 1–13.

Salomon, D., Ayalon, O., Patel-King, R., Hynes, R.O., and Geiger, B. (1992). Extrajunctional distribution of N-cadherin in cultured human endothelial cells. J. Cell Sci. *102*, 7–17.

Sarin, H. (2010). Physiologic upper limits of pore size of different blood capillary types and another perspective on the dual pore theory of microvascular permeability. J. Angiogenes Res. *2*, 14.

Schäfer, N.F., Luhmann, U.F., Feil, S., and Berger, W. (2009). Differential gene expression in Ndph-knockout mice in retinal development. Invest. Ophthalmol. Vis. Sci. *50*, 906–916.

Shearer, G.C., and Kaysen, G.A. (2006). Endothelial bound lipoprotein lipase (LpL) depletion in hypoalbuminemia results from decreased endothelial binding, not decreased secretion. Kidney Int. *70*, 647–653.

Simionescu, M., Simionescu, N., Silbert, J.E., and Palade, G.E. (1981). Differentiated microdomains on the luminal surface of the capillary endothelium. II. Partial characterization of their anionic sites. J. Cell Biol. *90*, 614–621.

Stadtfeld, M., and Graf, T. (2005). Assessing the role of hematopoietic plasticity for endothelial and hepatocyte development by non-invasive lineage tracing. Development *132*, 203–213.

Stan, R.V. (2004). Multiple PV1 dimers reside in the same stomatal or fenestral diaphragm. Am. J. Physiol. Heart Circ. Physiol. *286*, H1347–H1353.

Stan, R.V., Roberts, W.G., Predescu, D., Ihida, K., Saucan, L., Ghitescu, L., and Palade, G.E. (1997). Immunoisolation and partial characterization of endothelial plasmalemmal vesicles (caveolae). Mol. Biol. Cell *8*, 595–605.

Stan, R.V., Ghitescu, L., Jacobson, B.S., and Palade, G.E. (1999a). Isolation, cloning, and localization of rat PV-1, a novel endothelial caveolar protein. J. Cell Biol. *145*, 1189–1198.

Stan, R.V., Kubitza, M., and Palade, G.E. (1999b). PV-1 is a component of the fenestral and stomatal diaphragms in fenestrated endothelia. Proc. Natl. Acad. Sci. USA *96*, 13203–13207.

Stan, R.V., Arden, K.C., and Palade, G.E. (2001). cDNA and protein sequence, genomic organization, and analysis of cis regulatory elements of mouse and human PLVAP genes. Genomics *72*, 304–313.

Stan, R.V., Tkachenko, E., and Niesman, I.R. (2004). PV1 is a key structural component for the formation of the stomatal and fenestral diaphragms. Mol. Biol. Cell *15*, 3615–3630.

Tkachenko, E., Tse, D., Sideleva, O., Deharvengt, S.J., Luciano, M.R., Xu, Y., McGarry, C.L., Chidlow, J., Pilch, P.F., Sessa, W.C., et al. (2012). Caveolae,

fenestrae and transendothelial channels retain PV1 on the surface of endothelial cells. PLoS ONE *7*, e32655.

Tse, D., and Stan, R.V. (2010). Morphological heterogeneity of endothelium. Semin. Thromb. Hemost. *36*, 236–245.

Villaschi, S., Johns, L., Cirigliano, M., and Pietra, G.G. (1986). Binding and uptake of native and glycosylated albumin-gold complexes in perfused rat lungs. Microvasc. Res. *32*, 190–199.

Wisse, E. (1970). An electron microscopic study of the fenestrated endothelial lining of rat liver sinusoids. J. Ultrastruct. Res. *31*, 125–150.

Yoshino, G., Hirano, T., Nagata, K., Maeda, E., Naka, Y., Murata, Y., Kazumi, T., and Kasuga, M. (1993). Hypertriglyceridemia in nephrotic rats is due to a clearance defect of plasma triglyceride: overproduction of triglyceride-rich lipoprotein is not an obligatory factor. J. Lipid Res. *34*, 875–884.

Developmental Cell, Volume *23*

Supplemental Information

The Diaphragms of Fenestrated Endothelia:

Gatekeepers of Vascular Permeability

and Blood Composition

Radu V. Stan, Dan Tse, Sophie J. Deharvengt, Nicole C. Smits, Yan Xu, Marcus R. Luciano, Caitlin L. McGarry, Maarten Buitendijk, Krishnamurthy V. Nemani, Raul Elgueta, Takashi Kobayashi, Samantha L. Shipman, Karen L. Moodie, Charles P. Daghlian, Patricia A. Ernst, Hong-Kee Lee, Arief A. Suriawinata, Alan R. Schned, Daniel S. Longnecker, Steven N. Fiering, Randolph J. Noelle, Barjor Gimi, Nicholas W. Shworak, and Catherine Carrière

Inventory of Supplemental Information

Figure S1

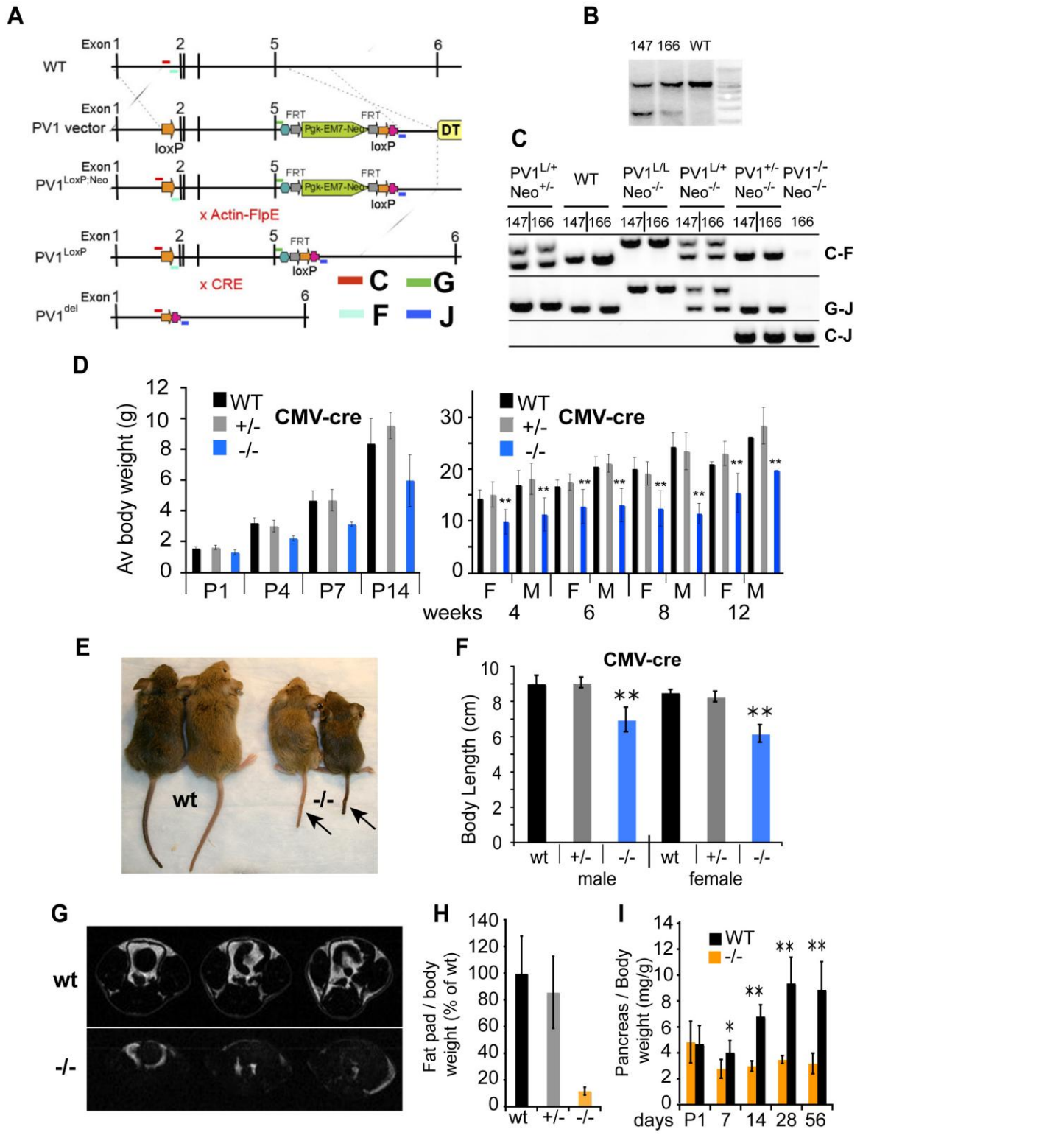

Figure S1: Targeting, validation and additional characterization of the PV1$^{-/-}$ phenotype.

A. Schematic of the wild-type PV1 locus (WT), features of the targeting construct (PV1 vector), *PV1*$^{LoxP;Neo}$ recombined locus, *PV1*^{LoxP} locus after deletion of the Neomycin selection cassette by the actin promoter -driven FLPe and deletion of *Plvap* exons 2-5 by the cre recombinase (PV1^{del}). The position of primers used for

genotyping is indicated. Primer pair C-F and G-J probe for the loxP sites whereas primer pair C-J demonstrates deletion of intervening sequence between the loxP sites.

B. Southern blotting on the two ES clones used to generate *PV1*$^{L/L}$ mice.

C. Genotyping of different steps in generation of *PV1*$^{-/-}$ mice.

D. Body weights of *PV1*$^{-/-}$, WT and *PV1*$^{+/-}$ littermates from 1 to 14 day-old (left) and from 4 to 12 week- (right) old mice. (n=4-8 per time point, *p<0.05, **p<0.01, stdev)

E-F. PV1$^{-/-}$ mice are smaller than their control littermates. Examples of 4 weeks old *PV1*$^{-/-}$ and WT littermates (E). Arrows show kinks in the tail of the *PV1*$^{-/-}$ mice, a finding that was very consistent. Comparison of snout-to-tail length in 8 week-old littermates (F). (n=4, **p<0.01, stdev)

G-H. *PV1*$^{-/-}$ mice have greatly diminished fat deposits as shown by (G) magnetic resonance imaging of abdominal fat in 3 consecutive slices at the same level in WT (upper) and *PV1*$^{-/-}$ mice (lower); (H) gonadal fat pad/body weight ratio in WT, *PV1*$^{+/-}$ and *PV1*$^{-/-}$ mice.

I. Decreased pancreas size as shown by diminished pancreas/body weight ratio in *PV1*$^{-/-}$ mice (orange) as compared to control littermates. (n=4-8 per time point, *p<0.05, **p<0.01, stdev).

Figure S2

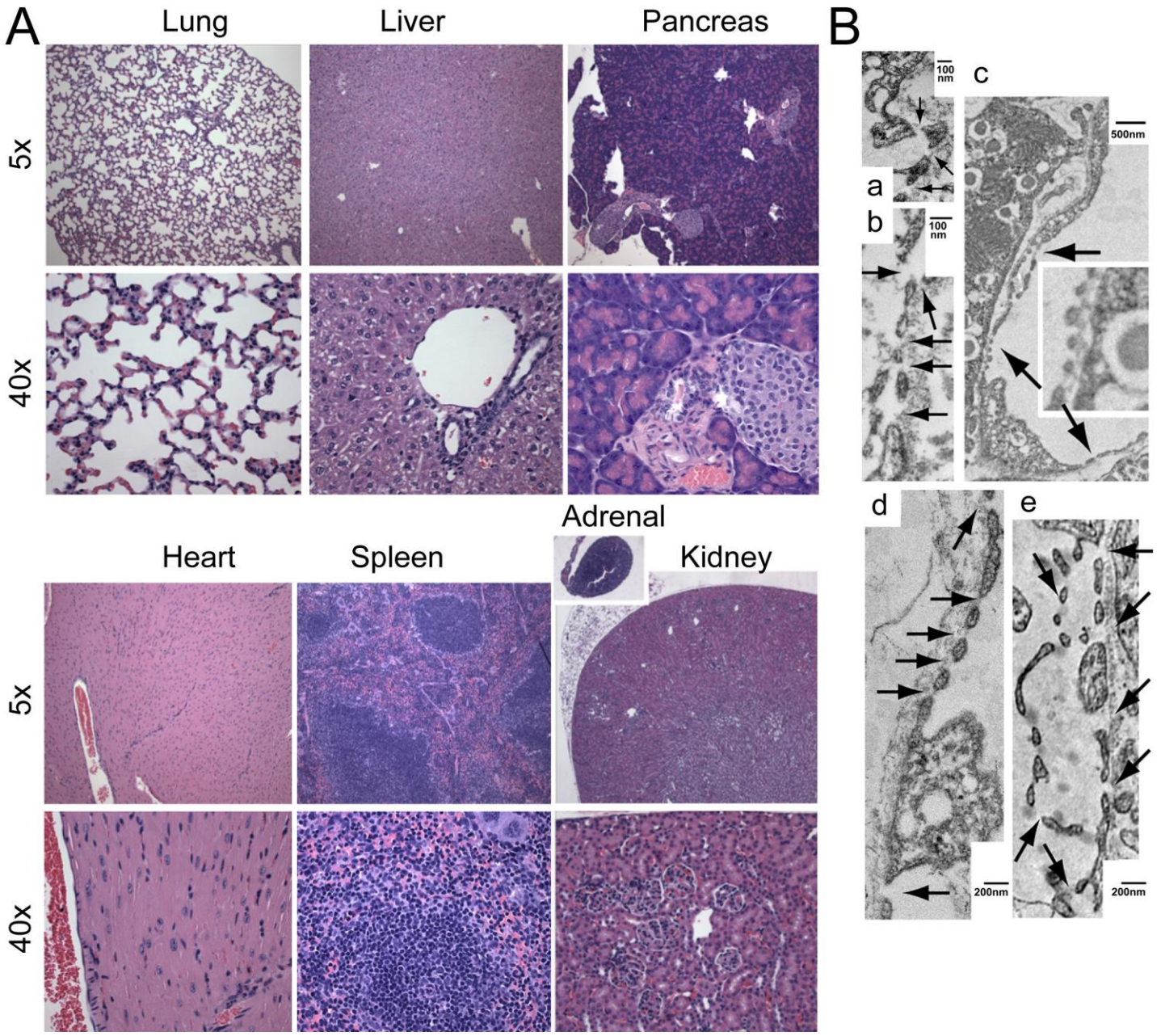

Figure S2: Additional characterization of the PV1$^{-/-}$ phenotype.

A**.** Histology of lung, liver, pancreas, heart, spleen, adrenal and kidney tissues in *PV1*$^{-/-}$ mice at 4 weeks. H&E staining of formalin fixed and paraffin embedded tissues. Magnification is indicated.

B. Transmission electron micrographs of capillaries from PV1$^{-/-}$ intestinal (jejunum) villus (**a**); choroid **(b**) pituitary **(c**) thyroid (**d**) and a kidney peritubular capillary in a newborn *PV1*$^{-/-}$ mouse on C57BL/6J background (**e**).

Figure S3

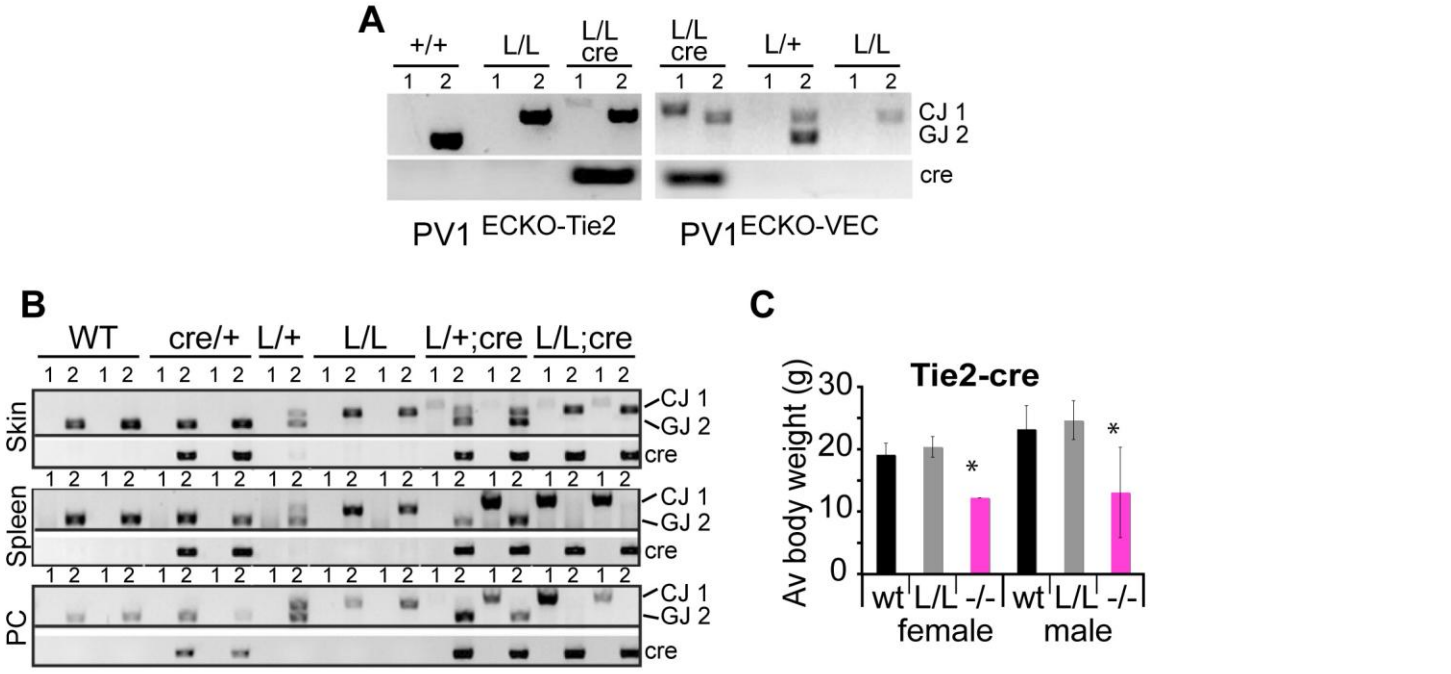

Figure S3: Validation and additional characterization of endothelial and hematopoietic- specific deletion of PV1.

A) Examples of genotyping of *PV1*$^{ECKO\text{-}Tie}$, *PV1*$^{ECKO\text{-}VEC}$ and *VEC-PV1HA* mice.

B) Genotyping carried out on genomic DNA extracted from skin, blood and peritoneal cells (PC) of *PV1*$^{HCKO\text{-}Vav1}$ mice and control littermates.

D) Body weight of *PV1*$^{ECKO\text{-}Tie2}$ mice compared to controls (n=4-8 per time point, *p<0.05, **p<0.01, stdev)

Figure S4

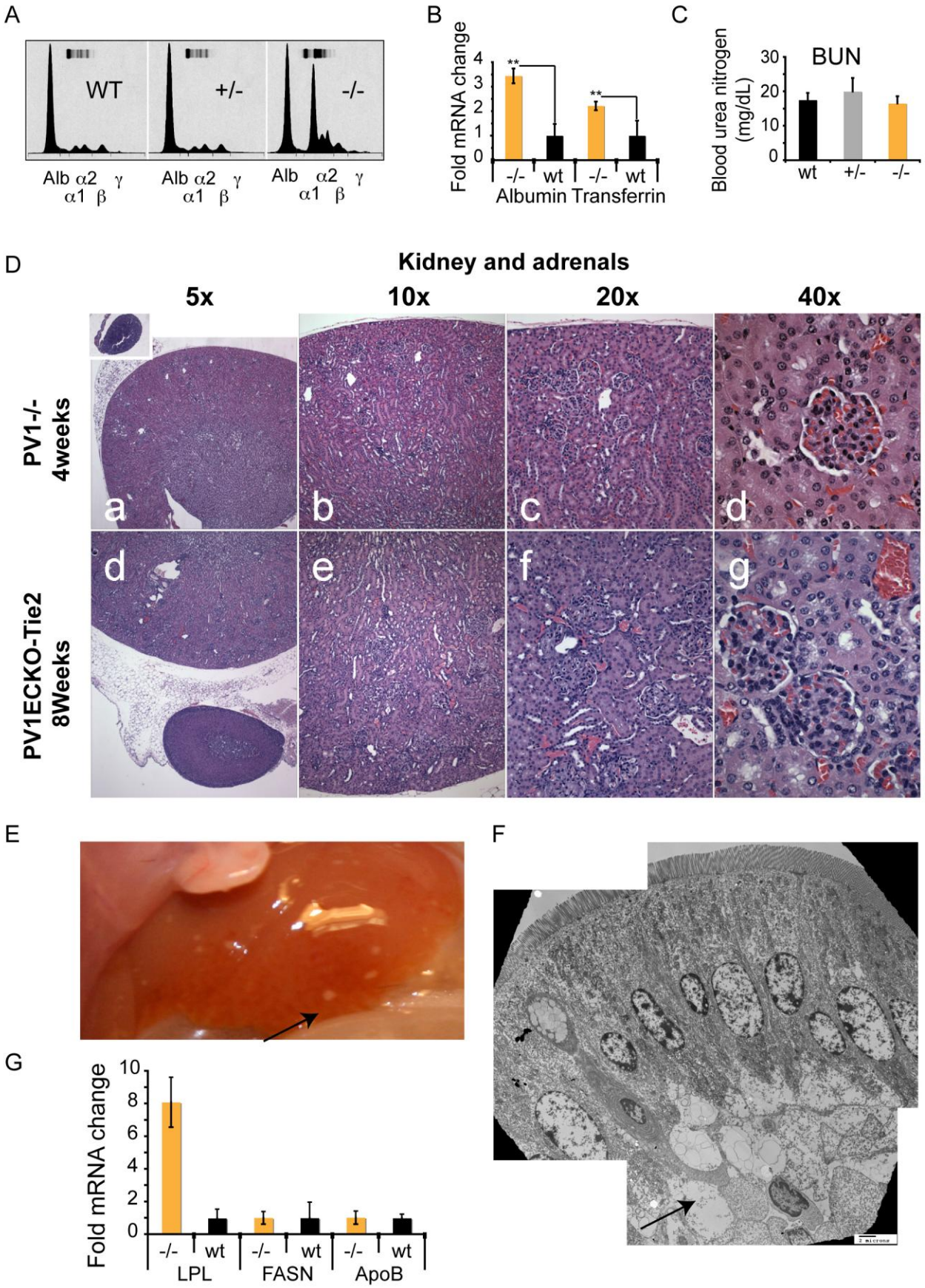

Figure S4: PV1 deletion results in disruption of blood homeostasis

A) Representative densitometry traces of the agarose gel electrophoresis resolved serum proteins from Figure 3 panel F.

B) Liver mRNA levels of albumin and transferrin are increased in *PV1*$^{-/-}$ compared to control littermates at 28 days, as determined by real time PCR. (n=4 for *PV1*$^{-/-}$, n=8 for WT)

C) Blood urea nitrogen (BUN) in 4 week-old *PV1*$^{-/-}$ and control littermates. (n<8)

D) H&E staining of kidney and adrenals from *PV1*$^{-/-}$ (a-d) and *PV1*$^{ECKO\text{-}Tie2}$ (e-h) mice at different ages.

E) Lipid deposits (xantoma) on the surface of the liver in a 10 week-old *PV1*$^{-/-}$ mouse.

F) Montage of low power electron micrographs of a PV1$^{-/-}$ intestinal vilus tip showing signs of edema, lipids and cellular damage.

G) Liver real-time PCR measured mRNA levels of apolipoprotein B mRNA (ApoB) and fatty acid synthase (Fasn) and lipoprotein lipase (Lpl) showing no change in the ApoB and Fasn message levels whereas Lpl is highly increased. (n=4 for *PV1*$^{-/-}$, n=8 for WT)

Figure S5

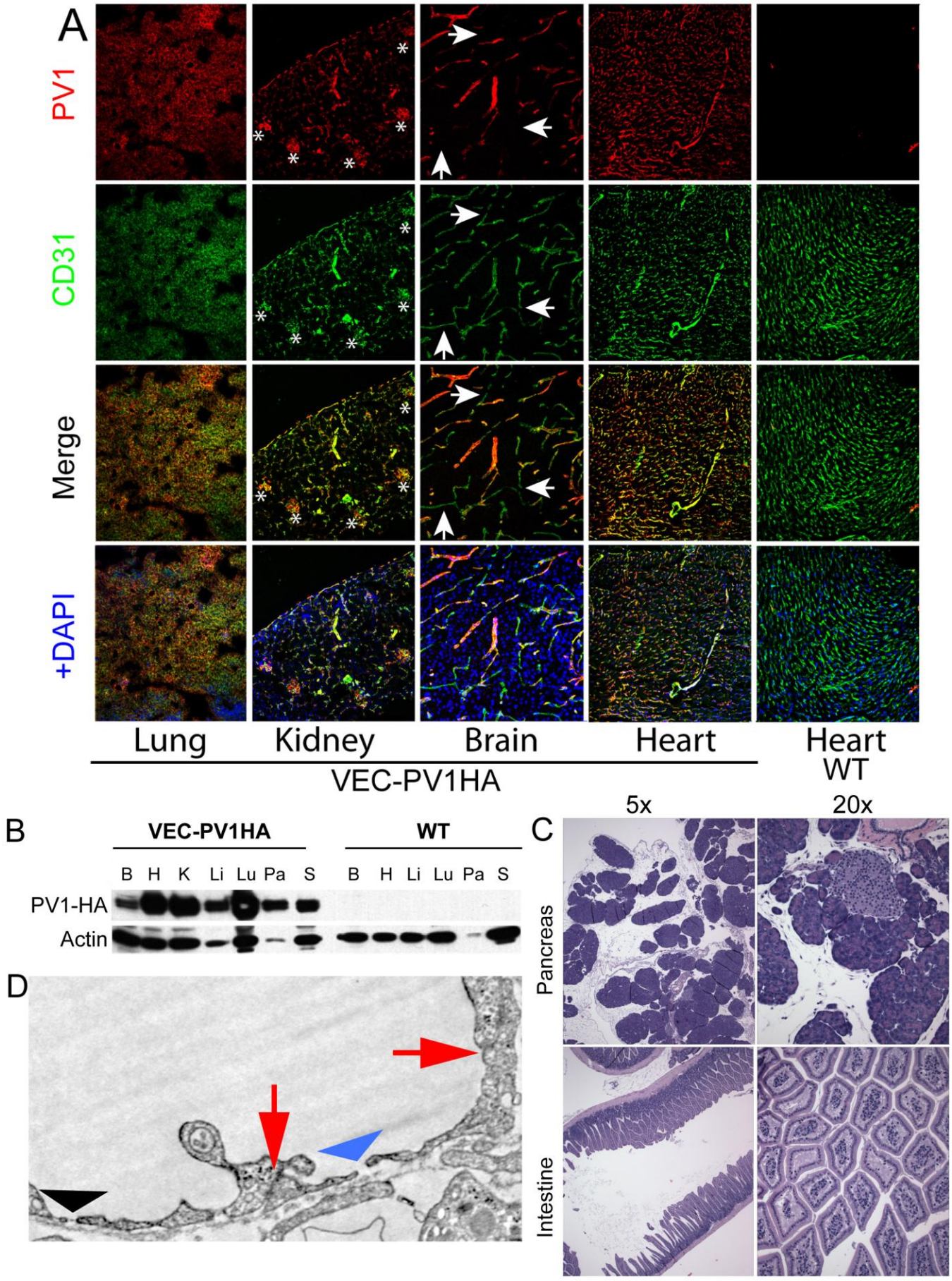
A
PV1
CD31
Merge
+DAPI
Lung
Kidney
Brain
Heart
Heart
WT
VEC-PV1HA
B
VEC-PV1HA
WT
B H K Li Lu Pa S
B H Li Lu Pa S
PV1-HA
Actin
C
5x
20x
Pancreas
Intestine
D

Figure S5: Endothelial specific reconstitution of PV1 rescues the PV$^{-/-}$ phenotype

A) Immunofluorescence with anti-PV1 (red) and anti-CD31 (green) antibodies on tissues from *VECPV1HA*$^{tg/+}$ mice and WT. Please note the extensive colocalization with CD31 in all tissues tested. PV1HA is also expressed in the heart, brain and kidney glomerulus (white asterisks) capillaries where PV1 is not natively expressed. Mosaicism of expression (white arrows in the brain micrographs) causes occasional vessels not to express the transgene. Scale bar 10μm.

B) Western blotting with anti-HA and anti-β-actin antibodies of total membrane proteins isolated from different tissues from *VEC-PV1HA*$^{tg/+}$ (left) and WT mice (right). B- brain, H– heart, K– kidney, Li– liver, Lu– lung, Pa– pancreas, Sp– spleen. Anti-β-actin blotting was performed on the same membrane after anti-HA.

C) H&E staining of formalin fixed paraffin embedded pancreas (left panels) and intestine (right panels) tissues in the ECRC mice. Magnification 5x (top panels) and 20x (bottom)

D) Electron micrograph of a PV1^{ECRC} kidney peritubular capillary demonstrating mosaicism of expression of the FDs. Two junctions (red arrows) separate the two ECs that contribute to the capillary wall. One EC has a fenestra lacking FD (blue arrowhead) whereas the other EC has a fenestra with FD (black arrowhead).

Supplemental Tables

Table S1 (relevant to Fig 3 and 5): Blood plasma comprehensive metabolic panel concentration values in 4 weeks old PV1$^{-/-}$, PV1$^{+/-}$ and WT mice.

		WT (n=5)		**PV1+/-** (n=9)		**PV1-/-** (n=9)		TTEST
Units	***Test***	*average*	*sd*	*average*	*sd*	*average*	*sd*	*p*
mg/dL	**Glucose**	320.8	76.9	339.4	52.0	248.5	60.1	1.22E-01
mg/dL	**BUN**	16.2	2.1	17.2	3.7	20.3	4.5	6.31E-02
mg/dL	**CREAT**	0.0	0.1	0.1	0.0	0.0	0.0	1.45E-01
mmol/L	**Na**	144.2	1.9	145.4	1.5	146.5	2.1	2.49E-01
mmol/L	**K**	5.2	1.2	4.8	1.4	5.5	1.6	6.59E-01
mmol/L	**Cl**	109.6	1.1	111.6	2.1	**118.0**	4.2	**1.68E-03
mmol/L	**CO2L**	19.4	2.1	18.2	2.3	22.0	1.4	7.61E-02
	AGAP	15.8	2.2	15.6	3.0	**7.0**	0.0	**6.93E-04
mg/dL	**CA**	9.6	0.4	9.6	0.3	**8.6**	0.1	**3.06E-03
mg/dL	**CHOL**	96.7	16.4	109.1	20.2	**182.3**	53.0	**3.26E-05
mg/dL	**TRIG**	72.9	14.5	77.6	32.7	**1880.8**	243.9	**4.47E-19
mg/dL	**HDLc**	78.4	13.9	86.2	13.8	**14.0**	0.0	**4.87E-05
g/dL	**TP**	4.1	0.1	4.0	0.1	**1.7**	0.1	**8.39E-11
g/dL	**Alb**	2.6	0.1	2.7	0.2	**0.9**	0.1	**1.81E-09
	A/G	1.8	0.1	2.0	0.2	**1**	0.1	**4.11E-04
U/L	**AST**	247.6	81.7	181.2	126.5	116.8	110.3	1.21E-01
U/L	**ALT**	116.0	98.8	91.8	79.5	48.0	35.3	2.33E-01
U/L	**ALP**	228.0	26.7	257.4	20.2	**86.5**	14.8	**1.65E-05
mg/dL	**TBIL**	0.4	0.2	0.2	0.1	**1.0**	0.8	*1.72E-02
mg/dL	**DBIL**	0.0	0.1	0.0	0.0	0.2	0.2	9.18E-02

BUN – blood urea nitrogen, CREAT – creatininine, Na – sodium, K – potassium, Cl – chloride anion, CO2 – bicarbonate, AGAP – anion gap, CHOL – total cholesterol, TG – triglycerides, HDLc – high density lipoprotein cholesterol, TP – total protein, Alb – serum albumin, A/G - albumin/globulin ratio, AST – aspartate aminotransferase, ALT – alanine aminotransferase, ALP – alkaline phosphatase, TBIL – total bilirubin, DBIL – direct bilirubin. sd – standard deviation. Statistical significance was calculated for values in the *PV1$^{-/-}$* mice versus wild type littermates using a two tailed Student's t test: * $p<0.05$, ** $p<0.01$. Number of mice: WT (n=5), PV1$^{+/-}$ (n=9), PV1$^{-/-}$ (n=9). The values that are significantly different in the PV1$^{-/-}$ mice are noted in bold face.

Table S2: Characteristics of the capillaries found in the organs used for permeability assay.

Organ	EC Types	Segment	SDs	FDs
Intestine	continuous	muscularis	NO	NO
	fenestrated	Villi	Yes	Yes
Pancreas	fenestrated	endocrine and exocrine	Yes	Yes
Kidney	fenestrated	peritubullar capillaries	Yes	Yes
	fenestrated	glomerulus	NO	NO
	continuous	vasa recta	Yes	NO
Lung	continuous	pulmonary capillaries	Yes	NO
Liver	discontinous	sinusoids	Yes	NO
Heart	continuous	all	NO	NO

Supplemental Experimental Procedures

Genetically modified mice and animal care:

Generation of PV1$^{L/L}$ mice: The PV1loxP targeting vector was constructed by Bacterial Artificial Chromosome (BAC) recombination technology ("recombineering") with the help of the BAC Engineering Core Facility, Neuroscience Center, U. North Carolina at Chapel Hill. The mouse BAC clone bMQ-264F22 (derived from AB2.2 ES cells, 129S7 mouse strain) containing the *PV1/Plvap* gene was obtained from The Wellcome Trust Sanger Institute (Cambridge, UK). A loxP recombination site was introduced in intron 1 via a loxP-PGKp-NeomycinR-loxP cassette. Upon induction of Cre recombinase expression, the PGK-Neo resistance gene cassette was excised leaving an "orphan" loxP site in intron 1. The plasmid was further modified by the insertion of FRT-PGK-EM7-NeoR-FTR-loxP cassette in intron 5 of the *PV1/Plvap* locus. The linearized targeting construct was electroporated into V6.5 embryonic stem (ES) cells (F1 of 129Sv/J and C67BL/6). Neomycin-resistant recombinant ES cells were PCR-genotyped for the presence of the orphan loxP site and for proper homologous recombination at both the 5' and 3' ends of the construct. Twenty clones positive by PCR genotyping were further genotyped by Southern blotting. Two clones (#147 and #166) were selected for embryo aggregation and generation of chimaera. The chimaeras were bred to wild-type C57Bl/6J mice to select for germline transmission. The positive offspring labeled *PV1$^{L/wt}$;Neo+/-* were further bred to a transgenic mouse expressing *FLPe* recombinase under the control of *ACTB* promoter in C57Black/6J background (strain B6.SJL-Tg(ACTFLPe)9205Dym/J) (Branda and Dymecki, 2004), this resulting in germline deletion of the PGK-Neo cassette generating the *PV1$^{L/wt}$* mice. *PV1$^{L/wt}$* mice were then interbred to obtain homozygous PV1$^{L/L}$ mice, which express PV1 at normal levels and have no overt phenotype.

Generation of PV1$^{-/-}$ mice: *PV1$^{L/+}$* mice were bred to *CMV-cre* mice (BALB/c-Tg(CMV-cre)1Cgn/J) to generate *PV$^{-/+}$* mice. These last mice were then intercrossed to generate *PV1$^{-/-}$* mice as well as the control littermates *PV1$^{-/+}$* and WT (Fig S1B).

Generation of endothelial- and hematopoietic-specific PV1 knockouts: *PV1$^{L/L}$* mice were crossed with *Tie2-cre* (Koni et al., 2001) and *VE-Cadherin-cre* (Chen et al., 2009) mice to generate *PV1$^{ECKO-Tie2}$* and *PV1$^{ECKO-VEC}$* mice in which PV1 is specifically deleted in both endothelial and hematopoietic cell lineages during embryogenesis. Crossing of the *PV1$^{L/L}$* mice with the *Vav1-cre* mice generated the *PV1$^{HCKO-Vav}$* mice in which PV1 is deleted only in the hematopoietic cell lineage, during embryogenesis.

Generation of VEC-PV1HA$^{tg/+}$ and PV1^{ECRC} mice: The construct mPV1-3xHA-IRES-hrGFP was previously described (Stan et al., 2004). The PV1HA was amplified using the following primers: 5' – AAAAGCATGCAAATGGGGCTCTCCAT-3' and 5'-AAAAGCGGCCGCTATTAAGCGTAGTCA–3' and subcloned in the SmaI and NotI sites of the pVECDp-GFP-5' Int1 construct (kind gift of Dr. Shin-Ichi Nishikawa, Kyoto University)(Hisatsune et al., 2005). VEC-PV1HA transgenic cassette consisting of the VEC promoter, PV1HA, SV40 polyA signal sequence and the 5' 5kb of the VE Cadherin intron 1 (Fig S1C) was injected in C57BL/6J ovocytes (Dartmouth Trangenics Facility). Six of the *VEC-PV1HA$^{tg/+}$* lines generated showed germline transmission. Genotyping was done using the following primers: Set 1 (Fig S1E) antisense 5'-GTC

GTT CCT GGC ACT GCT TCT CG-3' and sense 5'-GTG TGG CTC CCC TCT CCC CTC C-3' and Set 2 (Fig S1E) sense 5'-ACAAAGGAACAATAACAGGAAACC-3' and antisense 5' – CATTTTCACGGGTCACGC-3'. These clones were characterized in terms of expression pattern in the vessels of the mice, by Western blotting, microscopy and flow cytometry with anti-PV1 antibodies. The *VEC-PV1HA*$^{tg/+}$ mice were bred to *PV1*$^{+/-}$ mice and their progeny used to reconstitute PV1 specifically in endothelial cells, mice which were labeled *PV1*^{ECRC} (genotype *PV1*$^{-/-}$*;VEC-PV1HA*$^{tg/+}$).

*Speed Congenics***:** Heterozygous mice on mixed 129 and C57Bl/6 background were rapidly bred back to the C57Bl/6 background in five generations using marker analysis of genomic DNA to determine "best breeder". This was performed DartMouse™, the Dartmouth Mouse Speed Congenic Facility (www.DartMouse.com), using 1449 SNP arrays covering the mouse genome with an average interval density of < 5 cM. SNPs were queried by PCR using GoldenGate Genotyping (Illumina; San Diego, CA) and assessed using an Illumina BeadStation 500.

Antibodies used: rabbit anti-Cav1 and rat anti-mouse CD31 (MEC13.3) were from BD Pharmingen (San Diego, CA); goat anti-CD31 and goat anti-VE Cadherin from Santa Cruz Biotechnology (Santa Cruz, CA); mouse anti-ApoB (Nguyen et al., 2006) was a kind gift from Dr. Ross Milne (University of Ottawa Heart Institute). Rat anti-mouse PV1 (MECA-32 clone) (Hallmann et al., 1995; Keuschnigg et al., 2009) was affinity purified by FPLC on an anti-rat IgG column from the MECA-32 hybridoma supernatant grown in protein free media by BioXCell (Lebanon, NH). Chicken anti-mouse PV1C pAb was raised in chickens against a synthetic peptide (**KG** LPVVNPAAQPSG single letter code, mPV1C peptide) coupled to BSA. The mPV1C peptide consisted of the last 12 aa from mouse PV-1 C terminus, to which a glycine and a lysine (in bold) were added for increased solubility and coupling purposes, respectively. Eggs were collected after the fourth antigen boost and total IgY purification, affinity purification and antibody characterization were performed as described (Stan et al., 1999a; Stan et al., 2004). All fluorescently labeled $F(ab)_2$ antibody fragments were from Invitrogen - Molecular Probes (Carlsbad, CA); unlabeled and HRP-conjugated rabbit anti-chicken IgY and the goat anti-mouse IgG-HRP from Biodesign (Kennebunk, ME).

Primary antibody labeling with fluorophores:

Affinity purified primary antibodies rat anti-mouse PV-1 mAb clone MECA-32, chicken anti-mouse PV-1C pAb, mouse IgM, mouse IgG2 were labeled with either Alexa (488, 555, 568 or 647) fluorophores (Invitrogen, Carlsbad, CA) or DyLight (547 or 647) fluorophores (Pierce, Thermo-Fisher, Rockford, IL), as per manufacturer's instructions.

Scanning electron microscopy: was performed as in our previous work (Murakami et al., 2008).

RNA isolation and real-time quantitative PCR: The Gene Expression assays used were: PV1 (PV1/Plvap), albumin (Alb), fibrinogen alpha chain (Fga), fibrinogen beta chain (Fgb), transferrin (Trf), fatty acid synthase

(Fasn), lipoprotein lipase (Lpl), ApoB (Apob), ApoB editing enzyme (Apobec), VE Cadherin / cadherin 5 (Cdh5), platelet/endothelial cell adhesion molecule 1 / CD31 (Pecam1). The PCR was performed on ABI 7500 Real Time PCR System with SDS software. Actin B (ActB) was used as control. The comparative C_T method ($2^{-\Delta\Delta CT}$) of relative quantitation was used to compare different genotypes.

Isolation of mouse lung total membranes: Lung membrane lysates were obtained from mice of different genotypes as described (Stan et al., 1999b). Briefly, mice were anesthetized with a mixture of ketamine:xylazine:acepromazine (6:2:0.5) and the lungs were flushed free of blood by perfusion (5min, 25ºC) with oxygenated phenol-red free HBSS, via the pulmonary artery. The lungs were collected, weighed, minced and homogenized (20 strokes, Teflon pestle-glass Thomas type BB homogenizer) in an ice-cold buffer (1:4/w:v) containing 25mM Hepes, pH7.2, 250 mM sucrose, 2 mM $MgCl_2$ and a protease inhibitors cocktail (10 µg/ml each leupeptin, pepstatin, o-phenantrolin, E-64 and 1 mM PMSF). The homogenate was filtered through 53µm nylon net and centrifuged for 15 min at 500xg to yield a nuclei/cell debris pellet and a postnuclear supernatant (PNS). The PNS was further fractionated by centrifugation (1h, 4ºC, 100,000xg, using a TLA45 rotor) in a total membranes pellet and a cytosolic supernatant. The membrane pellet was solubilized in 200 µl 10mM Tris, pH 6.8, 0.5%SDS, and protease inhibitors. Protein concentration was determined by a BCA protein assay (Pierce, Rockford, IL/USA). Equal amounts of protein (20µg) were adjusted to 1x reducing SDS-PAGE sample buffer, boiled for 5min, resolved by 8% SDS-PAGE, transferred to PVDF membrane and probed by immunoblotting. Lung membrane lysates were obtained from WT, *PV1*$^{+/-}$, *PV1*$^{-/-}$, *PV1*$^{L/L}$, *PV1*$^{L/wt}$;*cre*$^{+/-}$, *PV1*$^{ECKO\text{-}Tie2}$, *PV1*$^{ECKO\text{-}VEC}$, *PV1*^{HCKO}, *VEC-PV1HA*$^{tg/+}$, and *PV1*^{ECRC} mice.

SDS-PAGE, silver staining and immunoblotting: Equal amounts of proteins were separated by SDS-PAGE and Coomassie or silver stained (Stan et al., 1999a) or were transferred to PVDF membranes (Stan et al., 1999a). ECL (Pierce, Rockford, IL) was used as a detection system and images acquired using a G:Box Chemi XT16 imaging system and GeneSnap software (Syngene, Frederick, MD). For quantitation assays, fluorescent secondary antibodies were also used and the results quantitated using a Typhoon fluorimager (Molecular Dynamics, Sunnyvale, CA).

Flow cytometry to determine the expression of PV1 on endothelia in *VEC-PV1HA*$^{tg/+}$, *PV1*$^{-/-}$, *PV1*^{ECKO}, *PV1*^{HCKO} and *PV1*^{ECRC} mice: Mouse tissues were flushed free of blood by total body perfusion with PBS via the left ventricle. Organs were excised, minced and treated (37ºC, 30min) with collagenase IV (Sigma) and DNAase in PBS followed by passage through a 70µm filter. After two washes in PBS, cells were stained with cocktails of anti-HA mAb, anti-PV1 mAb (MECA-32), anti-CD31 (MEC 13.3) or anti-VE Cadherin (BV13 or VECD1). Anti-CD45 (30-F11) was used as a pan hematopoietic marker.

Isolation of blood plasma and serum: Mice were anesthetized as described above or euthanized with CO_2. The thoracic cavity was opened and a nick was made in their right atrium. For plasma isolation, blood was

immediately collected with heparin coated capillary tubes (Thermo-Fisher) and transferred to lithium heparin coated Microtainer tubes (BD Biosciences) containing a gel separator. After gentle mixing, the samples were centrifuged at 6000xg for 15 min to obtain platelet-poor plasma. For serum, blood was collected in Microtainer tubes coated with clotting activators (BD Biosciences) and containing a gel separator. The blood was allowed to clot for at least 30min at RT before serum separation by centrifugation at 6000xg for 15 min.

Isolation of white blood cells: For hematopoietic cells, blood was collected in EDTA coated Microtainer tubes (BD Biosciences) with no separator. The samples were centrifuged at 2000xg for 15 min to pellet the blood cells. After removal of the plasma, the buffy coat was collected and subjected to red blood cell lysis. The white blood cells were collected as a pellet and used to isolate genomic DNA.

Isolation of peritoneum cells: Cells were harvested by peritoneal lavage using 5 ml of warm (37ºC) buffer containing 2%BSA, 10mM EDTA, 4U/ml sodium heparin in HBSS, collected by centrifugation (5min,RT, 300xg) resuspended in HSS and profiled to determine the content of CD45-expressing cells (usually >95%).

Isolation of bone marrow cells: Bone marrow was collected from the femurs of *PV1*$^{HCKO\text{-}Vav}$ and control mice by flushing the bones with HBSS. Cells were washed, passed though a 70µm filter and counted. Either CD45+, CD11b+ or CD3+ cells were isolated using MicroMacs kits (Myltenyi) and were used for genotyping.

Isolation of splenocytes: Spleens were dissociated by mechanical disruption through a 70µm mesh. Cells were centrifuged and red blood cells were lyzed. After lysis cells were washed twice, passed again through a 70µm filter and used for genotyping. This procedure yields <5% non-hematopoietic cells.

Plasma lipoprotein fractionation by FPLC: Plasma (200 µl) was isolated as described and loaded onto one analytical grade Superose 6 column (GE Healthcare, Piscataway, NJ) (total bed volume of 24 ml and void volume of 8 ml). Plasma was passed over the column at a flow rate of 0.25 ml/min, and 0.5-ml fractions were collected. Total cholesterol and TG concentration of each fraction was determined using commercial kits (BioAssay Systems, Hayward, CA) and plotted against elution fraction. The ApoB content of fractions was determined by Western blotting with an anti-ApoB antibody that recognizes both ApoB48 and ApoB100.

Urinalysis was performed using Chemstrip 10 SG Urine Test Strips (Roche) measuring bilirubin, blood, glucose, ketone, leukocyte, nitrite, pH, protein, specific gravity and urobilinogen.

Magnetic Resonance Imaging and fat volume determination: MRI was performed on a 7T Varian Unity Inova magnetic resonance spectrometer equipped with a triple axes gradients. Axial images were acquired using a quadrature coil and a spin echo sequence with TR = 1.5 s, TE = 9 ms, field-of-view = 4 cm × 4 cm,

acquisition matrix = 256 × 128, slice thickness = 1 mm and number of slices = 16. Mice were anesthetized using a mixture of isoflurane and air.

First, a proton spectrum was acquired on each mouse to determine the fat and water resonance frequencies. Then, a fat image was acquired by suppressing the water resonance frequency. Optimum water suppression was ensured by arraying the power of the suppression pulse and selecting the power level that eliminated the water signal. Images were reconstructed from the free-induction-decay data using Matlab (The Mathworks Inc., Natick, MA). The images were exported in jpeg format and then analyzed using ImageJ (imagej.nih.gov/ij). The fat images were then thresholded and binarized. Fat content was calculated using the software embedded measurement tool and recorded as a percentage of the total cross-sectional area of the mouse in the corresponding *slice*. Data were averaged over 16 slices for each mouse.

Histology, staining and image processing: Mouse organs were immediately removed after euthanasia, fixed in 10% buffered formalin for at least 24h and embedded in paraffin. Sections (4-5µm thick) were cut and stained either with hematoxyllin/eosin, toluidine blue, Masson's trichrome stain for collagen, or periodic acid-Schiff (PAS) for carbohydrates, following established protocols in the Dartmouth-Hitchcock Pathology Laboratory. For fat content analysis, organs were fixed for 24h in methanol-free 4% paraformaldehyde in PBS, followed by cryoembedding in OCT compound (Tissue-Tek). Frozen sections (10µm thick) were stained with OilRed O or Sudan IV. Tissue morphology was examined and image acquisition was performed either using a Leica DM4000 upright microscope equipped with a DFC425 camera driven by LAS Imaging Analysis software (Leica Microsystems) or an Olympus BX51 microscope and a Q-Fire camera (QImaging) driven by QCapture software. Images were analyzed with ImageJ. Scoring was conducted using blinded slides, and findings were peer-reviewed by a second pathologist for concordance.

Evans Blue dye extravasation assays: Evans blue dye (6,6'-[(3,3'-dimethyl [l,l'- biphenyl-4,4'-diyl) bis (azo)] bis [4-amino-&hydroxy- 1,3-napthalenedisulfonic acid] was obtained form Sigma Chemical, St. Louis, MO. Age and sex matched mice were injected intravenously with 100µl / 20g body weight of sterile 2% Evans blue dye, 6% mouse serum albumin (99.9% pure, MP Bio) in 0.9 % saline. The tracer was allowed to circulate for 1min and a 50 µl sample of blood was taken as reference. After the indicated amount of time the mice were euthanized. For experiments where the ascites and intestinal lumen content of EB were assessed, the abdominal cavity was opened and the ascites fluid collected with capillary tubes. A 10 cm length of intestine was isolated with ligatures and 1ml sterile PBS gently injected in the lumen with a syringe and harvested from the other end of the loop with another syringe. Then the intestines were opened and their content scored for a blue coloration. For experiments where the tissue retention of EB was measured, the thoracic cage was opened, left atrium incised, blood collected on heparin and the whole body perfused with sterile PBS through the left ventricle at 1ml/min. The time was calculated as to comprise 15 min from EB injection to start of the perfusion. Organs of interest were collected (5cm of duodenum, kidney, pancreas, heart, lungs, and liver), weighed and put in formamide for 48h at 55ºC. The amount of EB extracted in formamide was calculated

against a standard curve of known EB concentrations by measuring the OD at 620 and 740nm using a spectrophotometer (Bio-Tek). The amount of EB retained was corrected to the initial EB concentration in the plasma expressed as µg/g tissue /15min. The ratio of initial (2min) and final (15min) plasma concentrations were calculated to determine the rate of leakage as well tissue/plasma ratio to determine retention.

Supplemental References

Branda, C.S., and Dymecki, S.M. (2004). Talking about a revolution: The impact of site-specific recombinases on genetic analyses in mice. Dev Cell *6*, 7-28.

Chen, M.J., Yokomizo, T., Zeigler, B.M., Dzierzak, E., and Speck, N.A. (2009). Runx1 is required for the endothelial to haematopoietic cell transition but not thereafter. Nature *457*, 887-891.

Ghitescu, L., Galis, Z., Simionescu, M., and Simionescu, N. (1988). Differentiated uptake and transcytosis of albumin in successive vascular segments. J Submicrosc Cytol Pathol *20*, 657-669.

Hallmann, R., Mayer, D.N., Berg, E.L., Broermann, R., and Butcher, E.C. (1995). Novel mouse endothelial cell surface marker is suppressed during differentiation of the blood brain barrier. Dev Dyn *202*, 325-332.

Hisatsune, H., Matsumura, K., Ogawa, M., Uemura, A., Kondo, N., Yamashita, J.K., Katsuta, H., Nishikawa, S., and Chiba, T. (2005). High level of endothelial cell-specific gene expression by a combination of the 5' flanking region and the 5' half of the first intron of the VE-cadherin gene. Blood *105*, 4657-4663.

Keuschnigg, J., Henttinen, T., Auvinen, K., Karikoski, M., Salmi, M., and Jalkanen, S. (2009). The prototype endothelial marker PAL-E is a leukocyte trafficking molecule. Blood *114*, 478-484.

Koni, P.A., Joshi, S.K., Temann, U.A., Olson, D., Burkly, L., and Flavell, R.A. (2001). Conditional vascular cell adhesion molecule 1 deletion in mice: impaired lymphocyte migration to bone marrow. J Exp Med *193*, 741-754.

Murakami, M., Nguyen, L.T., Zhuang, Z.W., Moodie, K.L., Carmeliet, P., Stan, R.V., and Simons, M. (2008). The FGF system has a key role in regulating vascular integrity. J Clin Invest *118*, 3355-3366.

Nguyen, A.T., Braschi, S., Geoffrion, M., Fong, L.G., Crooke, R.M., Graham, M.J., Young, S.G., and Milne, R. (2006). A mouse monoclonal antibody specific for mouse apoB48 and apoB100 produced by immunizing "apoB39-only" mice with mouse apoB48. Biochim Biophys Acta *1761*, 182-185.

Stan, R.V., Ghitescu, L., Jacobson, B.S., and Palade, G.E. (1999a). Isolation, cloning, and localization of rat PV-1, a novel endothelial caveolar protein. J Cell Biol *145*, 1189-1198.

Stan, R.V., Kubitza, M., and Palade, G.E. (1999b). PV-1 is a component of the fenestral and stomatal diaphragms in fenestrated endothelia. Proc Natl Acad Sci U S A *96*, 13203-13207.

Stan, R.V., Tkachenko, E., and Niesman, I.R. (2004). PV1 is a key structural component for the formation of the stomatal and fenestral diaphragms. Mol Biol Cell *15*, 3615-3630.

Tkachenko, E., Tse, D., Sideleva, O., Deharvengt, S.J., Luciano, M.R., Xu, Y., McGarry, C.L., Chidlow, J., Pilch, P.F., Sessa, W.C.*, et al.* (2012). Caveolae, fenestrae and transendothelial channels retain PV1 on the surface of endothelial cells. PloS one *7*, e32655.